APPLIED SCIENCES AND ENGINEERING

Nanoscale covalent organic framework-mediated pyroelectrocatalytic activation of immunogenic cell death for potent immunotherapy

Xingguang Li[1]*†, Meng-Lu Gao[1]†, Shan-Shan Wang[1], Yizhi Hu[1], Dongzhi Hou[1], Pei-Nian Liu[1,2]*, Huijing Xiang[3]*

Copyright © 2024 The Authors, some rights reserved; exclusive licensee American Association for the Advancement of Science. No claim to original U.S. Government Works. Distributed under a Creative Commons Attribution NonCommercial License 4.0 (CC BY-NC).

The conventional molecular immunogenic cell death (ICD) inducers suffer from poor biocompatibility and unsatisfactory efficacy. Here, a biocompatible nanosized covalent organic framework (nCOF)–based pyroelectric catalyst (denoted as TPAD-COF NPs) is designed for pyroelectric catalysis-activated in situ immunotherapy. TPAD-COF NPs confine organic pyroelectric molecules to rigid TPAD-COF NPs to substantially reduce aggregation and enhance biocompatibility, thus improving pyroelectrocatalytic efficiency. After tumor internalization, TPAD-COF NPs facilitate photothermal tumor ablation under near-infrared (NIR) laser exposure, resulting in effective ICD induction. In addition, TPAD-COF NPs effectively catalyze the conversion of temperature changes to pyroelectric changes, which subsequently react with adjacent O_2 to generate reactive oxygen species, thus triggering robust ICD activation. In vivo evaluation using mouse models confirmed that TPAD-COF NPs evidently inhibited the proliferation of primary and distant tumors and prevented lung metastasis under NIR laser illumination. Therefore, this study opens an avenue for designing nCOF-based catalysts for pyroelectric catalysis-activated in situ immunotherapy.

INTRODUCTION

Pyroelectric catalysis using pyroelectric biomaterials can catalyze the conversion of temperature changes into pyroelectric changes under alternating near-infrared (NIR) laser irradiation, which subsequently interact with O_2 to produce reactive oxygen species (ROS) (*1*, *2*). Studies have shown that inorganic pyroelectric nanoplatforms, such as $Bi_{0.5}Sb_{1.5}Te_3/CaO_2$ nanosheets (BST/CaO_2 NSs) and $Bi_{13}S_{18}I_2$ nanorods, can achieve effective photothermal and pyroelectric conversion for pyroelectric dynamic therapy (PEDT), resulting in notable tumor suppression and reduced thermal resistance of conventional photothermal therapy (PTT) (*3*, *4*). However, metal-related toxicity, low abundance, and inferior biodegradability of inorganic pyroelectric biomaterials severely hampered the application of NIR-triggered PEDT in tumor therapy (*5*–*8*). Therefore, the development of organic pyroelectric nanoplatforms is of crucial importance to circumvent the inherent drawbacks of PTT and improve the biocompatibility of PEDT treatment for potential clinical translation.

As an emerging category of crystalline and porous scaffolds, nanosized covalent organic frameworks (nCOFs) are composed of versatile organic monomers, which are linked by covalent bonds, and manifest exceptional performance in catalysis (*9*–*11*). The homogeneous pore size distribution and extremely high surface area render them as intriguing nanoplatforms for metal catalysis such as CO_2 reduction, coupling reactions, oxygen reduction, and so on (*12*–*17*). The structural tunability and rigidity of nCOFs provide a valid strategy to maximize the exposure of the catalytically active sites close to the substrate, thereby improving the catalytic efficiency (*18*, *19*). In addition, capitalizing on robust covalent bonds, nCOFs have excellent chemical stability and high biocompatibility, which is beneficial as a potential candidate nanoplatform for catalysis in biomedical application (*20*–*24*). Therefore, it is urgently needed to engineer pyroelectric nCOFs using organic pyroelectric molecules as the building blocks to improve the efficiency of pyroelectric catalysis and facilitate more efficient pyroelectric conversion, thereby leading to enhanced PEDT efficacy.

Recently, we and others have demonstrated that the use of pyroelectric biomaterials can catalyze the conversion of NIR laser into ROS to eradicate local tumors (*25*–*27*). However, such PEDT modality only works for locally irradiated tumors. Actually, cancer cells typically manifest extensive metastasis and recurrence, which seriously limits the treatment efficacy and leads to more than 90% of cancer-associated deaths (*28*, *29*). Immunotherapy has been acknowledged as a promising modality to eliminate tumor metastasis and recurrence (*30*–*34*). However, the treatment efficacy is severely restricted by low response rates (*35*). Several adjuvant treatment modalities, including chemotherapy, phototherapy, and radiotherapy, have been shown to cause immunogenic cell death (ICD), which can improve the rate of immune response, resulting in prominent therapeutic outcomes for metastatic tumors (*36*–*40*). The treatment efficacy largely relies on the efficiency of ICD inducers (*41*). Conventional molecular ICD inducers, such as oxaliplatin and indocyanine green (ICG), are often compromised by poor aqueous solubility and undesirable aggregation (*42*, *43*). Therefore, we hypothesize whether ligating a molecular pyroelectric ICD inducer into the porous structures of nCOFs can provide an effective approach to address these issues, effectively inducing ICD and eliciting cancer immunotherapy.

Here, we engineered a two-dimensional nCOF (denoted as TPAD-COF NPs) with the stacking of organic pyroelectric molecules for augmented pyroelectroimmunotherapy (Fig. 1). TPAD-COF NPs confined organic pyroelectric molecules in the rigid TPAD-COF NPs to reduce aggregation and improve biocompatibility, thus enhancing the efficiency of pyroelectric catalysis for more efficient pyroelectric conversion. After tumor accumulation, TPAD-COF NPs induced an apparent temperature elevation for photothermal ablation, leading to

[1]Shanghai Key Laboratory of Functional Materials Chemistry, Key Laboratory for Advanced Materials, School of Chemistry and Molecular Engineering, East China University of Science and Technology, Shanghai, 200237 China. [2]State Key Laboratory of Natural Medicines, School of Pharmacy, China Pharmaceutical University, Nanjing 210009, China. [3]School of Life Sciences, Shanghai University, Shanghai 200444, China.
*Corresponding author. Email: lixingguang@ecust.edu.cn (X.L.); liupn@ecust.edu.cn (P.-N.L.); xianghuijing@shu.edu.cn (H.X.)
†These authors contributed equally to this work.

effective ICD stimulation. In addition, TPAD-COF NPs effectively catalyzed the conversion of temperature changes into pyroelectric charges, which then interacted with adjacent O_2 to produce abundant ROS, thereby eliciting robust ICD activation. In vivo evaluation using distant tumor and lung metastasis models demonstrated that TPAD-COF NP administration notably suppressed primary and distant tumor growth and apparently retarded lung metastasis under NIR laser exposure. RNA profiling indicated that pathways related to apoptosis, metastasis and immune response were apparently enriched in the TPAD-COF NPs + laser group, including the forkhead box O (FOXO) signaling pathway, tumor necrosis factor (TNF) signaling pathway, Janus kinase–signal transducers and activators of transcription (JAK-STAT) signaling pathway, and major histocompatibility complex class I (MHC-I) and MHC-II pathways. Therefore, our work provided a distinct paradigm for the design of a nCOF-based pyroelectric catalyst to improve the biocompatibility and boost the therapeutic efficacy of immunotherapy.

RESULTS

Fabrication and characterization of TPAD-COF NPs

TPAD-COF was fabricated via the poly-condensation of 1,4,5,8-tetrakis((4-(5,5-dimethyl-1,3-dioxan-2-yl)phenyl)amino)anthracene-9,10-dione (TPAD-DMO) and 1,4,5,8-tetrakis((4-aminophenyl) amino) anthraxcene-9,10-dione (TPAD-NH_2) under solvothermal conditions (Fig. 2A). The x-ray diffraction (XRD) pattern of TPAD-COF NPs displayed strong and weak peaks at 4.65° and 9.30°, respectively, which were assigned to the (110) and (220) characteristic peaks (Fig. 2B). The porosity of TPAD-COF was investigated by N_2 isotherm, and the Brunauer-Emmett-Teller surface area was calculated to be 235 $m^2 g^{-1}$ (Fig. 2C). Compared to the precursors (TPAD and TPAD-NH_2), a new characteristic stretching vibration of C═N bond (1680 cm^{-1}) appeared in the Fourier transform infrared (FTIR) spectrum of TPAD-COF, which validated the successful formation of imine bonds in the TPAD-COF structure (Fig. 2D). To enhance the aqueous solubility and biocompatibility of TPAD-COF, the biocompatible amphiphilic polymer, 1,2-distearoyl-*sn*-glycero-3-phosphoethanolamine (polyethylene glycol) amine (DSPE-PEG-NH_2) was used to modify the surface of TPAD-COF to construct TPAD-COF NPs (figs. S1 to S11). The zeta potentials of DSPE-PEG-NH_2 and TPAD-COF NPs were −18.8 and −23.4 mV, respectively, confirming the successful fabrication of TPAD-COF NPs (Fig. 2E). Transmission electron microscopy (TEM) image of TPAD-COF revealed a rod-like morphology with a size of 100 nm (Fig. 2F). Dynamic light scattering (DLS) analysis exhibited that the hydrodynamic size of TPAD-COF NPs was approximately 120 nm (Fig. 2G). We also recorded the hydrodynamic size of various doses of TPAD-COF NPs in phosphate-buffered saline (PBS) solution to verify the assembly behavior. After assembling TPAD-COF (50, 100, and 200 μg ml^{-1}), the particle sizes were determined to be approximately 90 to 130 nm (fig. S12). The size and polydispersity

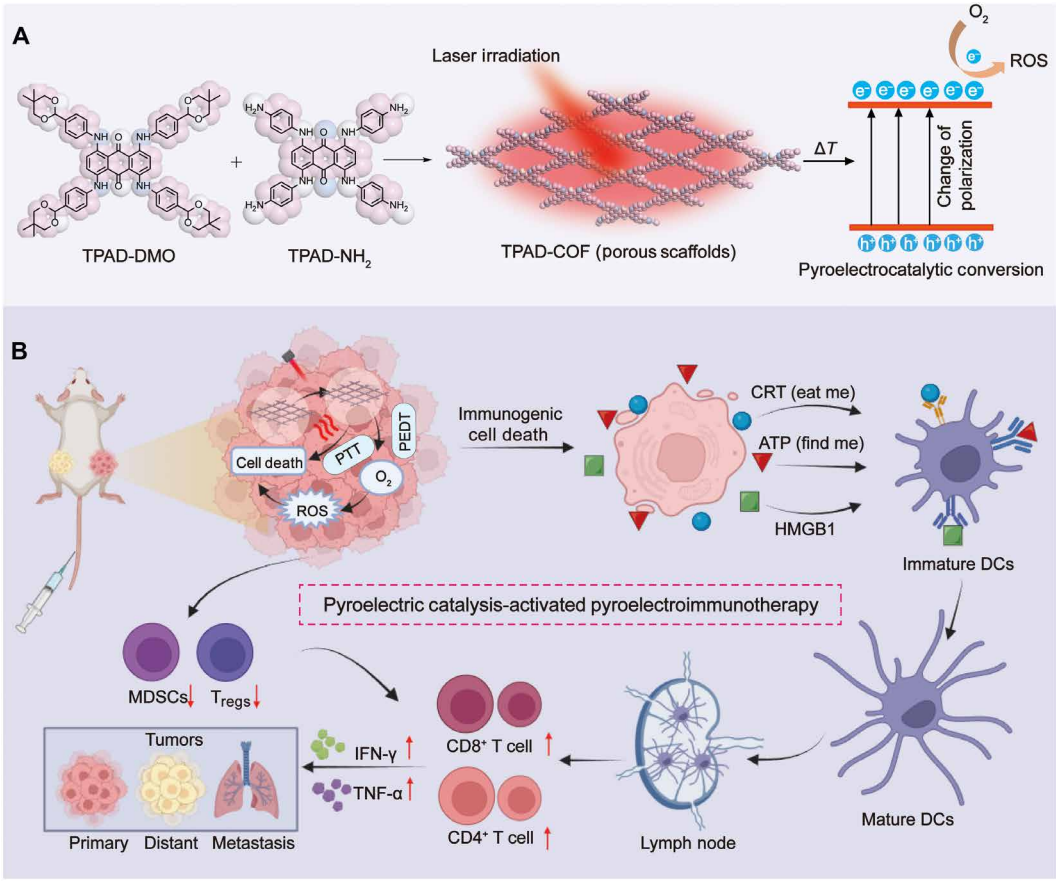

Fig. 1. Schematic illustration of TPAD-COF NP-mediated PEDT for tumor treatment and lung metastasis inhibition. (**A** and **B**) Schematic diagram of (A) the fabrication of TPAD-COF NPs and (B) their application in pyroelectric catalysis-activated immunotherapy.

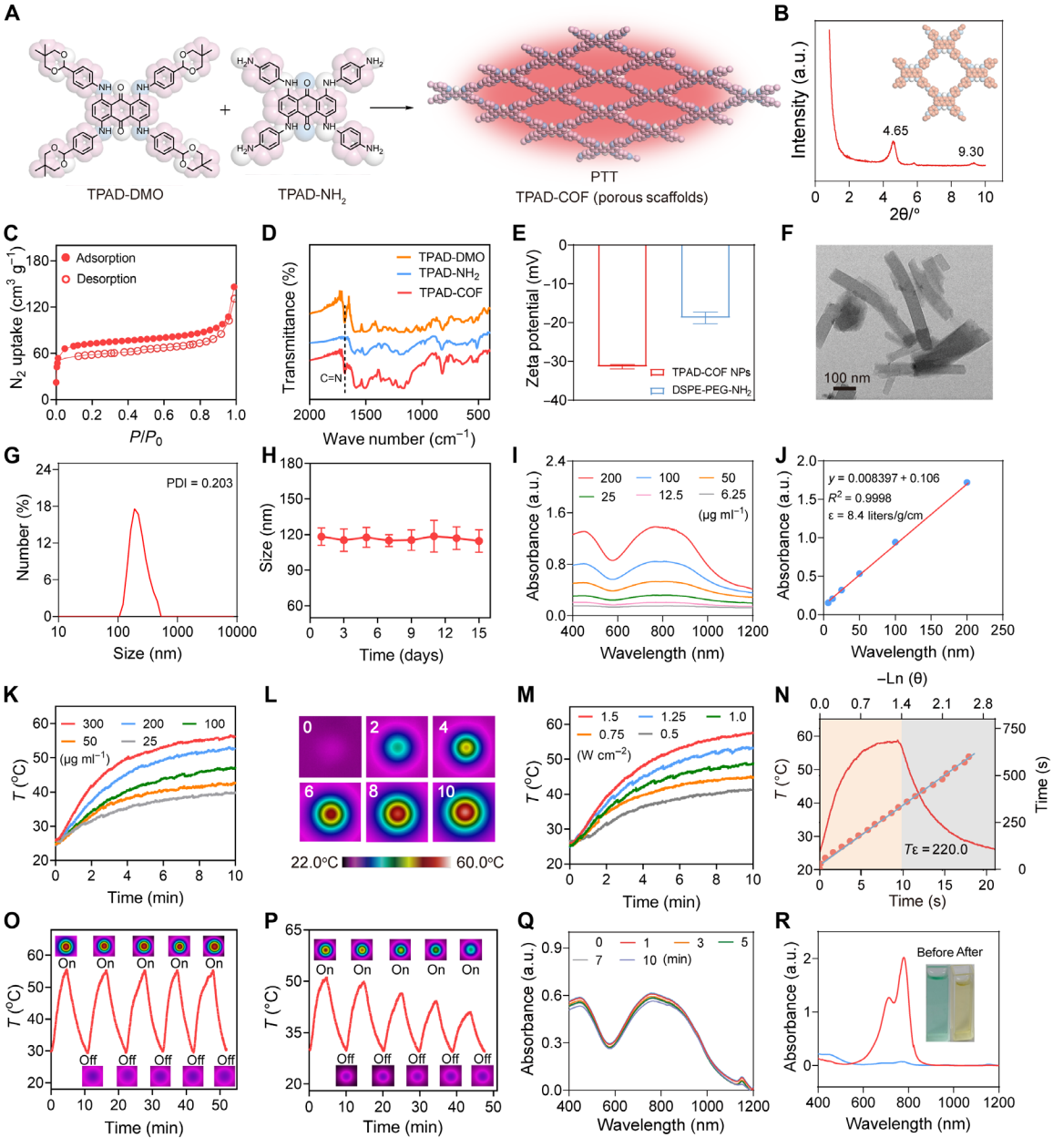

Fig. 2. Characterization of TPAD-COF NPs. (**A**) Synthetic route of TPAD-COF NPs. (**B**) XRD profile of TPAD-COF. (**C**) Nitrogen isotherm of TPAD-COF at 77 K. (**D**) FTIR spectra of TPAD-DMO, TPAD-NH_2, and TPAD-COF. (**E**) Zeta potential of TPAD-COF NPs (100 μg ml^{-1}) and DSPE-PEG-NH_2 ($n = 3$). (**F**) TEM image of TPAD-COF NPs. Scale bar, 100 nm. (**G**) Size distribution of TPAD-COF NPs (100 μg ml^{-1}) in PBS by DLS analysis. (**H**) Stability of TPAD-COF NPs (100 μg ml^{-1}) in PBS for 2 weeks ($n = 3$). (**I**) Ultraviolet-visible (UV-vis) absorption spectra of different doses of TPAD-COF NPs. (**J**) Fitting curve of absorbance of TPAD-COF NPs at 808 nm versus doses of TPAD-COF NPs. (**K**) Photothermal curves of various concentrations of TPAD-COF NPs under NIR laser irradiation (1.5 W cm^{-2}). (**L**) Thermal images of TPAD-COF NPs under NIR laser irradiation for various durations. (**M**) Photothermal curves of TPAD-COF NPs (300 μg ml^{-1}) irradiated by a NIR laser at diverse power densities. (**N**) Photothermal conversion capability of TPAD-COF NP dispersion (300 μg ml^{-1}) and linear time constant calculated from the cooling period (1.5 W cm^{-2}). (**O** and **P**) Photothermal curves and corresponding thermal images of (O) TPAD-COF NPs (300 μg ml^{-1}) and (P) ICG solution (300 μg ml^{-1}) under alternating NIR laser exposure (1.5 W cm^{-2}). (**Q** and **R**) UV-vis absorption spectra of (Q) TPAD-COF NPs (100 μg ml^{-1}) and (R) ICG solution (100 μg ml^{-1}) and corresponding photograph before and after NIR laser illumination (1.5 W cm^{-2}) for different durations. PDI, polydispersity index; a.u., arbitrary units.

index of TPAD-COF NPs in different solutions remained stable and did not change obviously during the 15-day observation, indicating that TPAD-COF NPs were highly stable under physiological conditions (Fig. 2H and figs. S13 to S15). Moreover, there was no marked change in the characteristic absorbance of TPAD-COF NPs over 15 days under different conditions, further proving the high stability of TPAD-COF NPs (fig. S16). In addition, different doses of TPAD-COF NPs exhibited substantial absorbance in the NIR region, and the mass extinction coefficient at 808 nm was 8.4 liters g^{-1} cm^{-1}, which further illustrated the potential application of TPAD-COF NPs in eliciting photothermal conversion (Fig. 2, I and J). The fluorescence emission spectra for TPAD-COF

and TPAD-COF NPs were also recorded, with similar fluorescence emission observed at 838 nm (fig. S17).

Inspired by the extensive absorption of TPAD-COF NPs in the NIR region, we explored their photothermal conversion performance under NIR laser exposure. After 10 min of laser exposure, the temperature of TPAD-COF NP aqueous solution at 300 μg ml^{-1} elevated rapidly from 25.2° to 56.6°C ($\Delta T = 31.4$°C) under NIR laser irradiation (Fig. 2, K and L). In addition, the temperature of TPAD-COF NP solution could be regulated from 41.2 to 57.5°C by increasing the laser power density from 0.5 to 1.5 W cm^{-2} (Fig. 2M). These findings showed that the temperature increment of TPAD-COF NP solution exhibited dose-dependent and power density–dependent patterns. The photothermal-conversion efficiency of TPAD-COF NPs at 808 nm was 29.1%, which is obviously higher than those of previously reported photothermal nanoplatforms, including Au nanorods (21%) (*44*) and $Cu_{2-x}Se$ nanocrystals (22%) (Fig. 2N) (*45*). Notably, the temperature variations were negligible after 5 cycles of alternating NIR laser exposure (Fig. 2O). In contrast, the temperature increment of ICG solution decreased obviously from 51.8° to 41.2°C after 5 heating and cooling cycles, demonstrating the photothermal stability of TFAD-COF NPs under NIR laser exposure (Fig. 2P). In addition, no apparent change in the absorption of TPAD-COF NPs was observed after 10 min of 808-nm laser exposure (Fig. 2Q). In comparison, the maximum absorbance of ICG solution decreased sharply after NIR laser exposure for 10 min, demonstrating the high photostability of TPAD-COF NPs (Fig. 2R).

Pyroelectric properties and ROS generation of TPAD-COF NPs

Inspired by the excellent photothermal effect and photostability of TPAD-COF NPs, their pyroelectric effect under 808-nm laser exposure was investigated by an electrochemical workstation. As shown in Fig. 3A, the temperature change causes the atomic motion of pyroelectric materials, resulting in a change in the polarization of the built-in pyroelectric field. Under NIR laser irradiation, the electric dipole moment decreases with increasing temperature ($dT/dt > 0$), thereby reducing the polarization strength of pyroelectric materials. The direction of the pyroelectric field coincides with that of the built-in electric field, which increases the transient short-circuit current. Conversely, when the laser is turned off, the temperature declines ($dT/dt < 0$), and the direction of the pyroelectric field is opposite to that of the built-in electric field, resulting in an opposite pyroelectric current (*46*). As expected, obvious pyroelectric currents and potentials of TPAD-COF NPs were observed under alternating NIR laser exposure, confirming that TPAD-COF NPs converted temperature changes into pyroelectric charges (Fig. 3, B and C). Further investigation of the electrochemical impedance spectra (EIS) of TPAD-COF NPs showed a slight reduction in the degree of electron transfer under 808-nm laser irradiation, illustrating the effective electron transfer of TPAD-COF NPs under NIR laser irradiation (Fig. 3D). Furthermore, the Mott-Schottky curves of the flat band potential of TPAD-COF NPs were studied (Fig. 3E). The conductive band (CB) of TPAD-COF was −1.245 V, which was calculated from the flat-band potential of TPAD-COF NPs (−1.39 V compared to a standard calomel electrode). The CB bandgap of TPAD-COF NPs was more negative than the redox potential of $O_2/{}^{\bullet}O_2^-$ (−0.54 V versus normal hydrogen electrode, pH 7), which was conducive to the efficient reduction of O_2 to ${}^{\bullet}O_2^-$ for ROS generation.

Density functional theory (DFT) calculations indicated that the energy gap between the highest occupied molecular orbital (HOMO) and lowest unoccupied molecular orbital (LUMO) of TPAD-COF (0.694 eV) was smaller than those of the precursors, TPAD-DMO (0.931 eV) and TPAD-NH_2 (0.832 eV), resulting in a redshift in the absorption spectrum of TPAD-COF (Fig. 3F). In addition, the electronic band structure of TPAD-COF NPs displayed that its bandgap is 0.541 eV, which is comparable to that of semiconductors (Fig. 3G). Consistently, ultraviolet-visible (UV-vis) diffuse reflectance analysis revealed an obvious redshift in the absorption of TPAD-COF compared to its precursors (Fig. 3H and fig. S18). In addition, a Tauc plot of the modified Kubelka-Munk function was used to identify the bandgap energy, which corresponds to the *x* intercept of the extrapolated linear portion of the plot (Fig. 3I). The bandgaps of TPAD-NH_2, TPAD-DMO and TPAD-COF were 1.41, 1.42, and 1.1 eV, respectively. Compared to TPAD-NH_2 and TPAD-DMO, the narrower bandgap of TPAD-COF would facilitate the charge-carrier pair separation, thereby promoting ROS generation under NIR laser illumination (Fig. 3J).

It has been confirmed that ROS, especially singlet oxygen ($^1O_2$), is produced on the surface of thermoelectric materials through the effective pyroelectric charge transfer under alternating heating and cooling. The $^1O_2$ generation capacity of TPAD-COF NPs under NIR laser exposure was evaluated using 1,3-dipenylisobenzofuran (DPBF) as the probe (Fig. 3K). After 10 min of NIR laser illumination, the absorbance of the DPBF solution containing TPAD-COF NPs rapidly decreased to approximately 60% of the original absorbance, while the absorption intensity of DPBF did not decrease apparently in the PBS- and NIR laser–treated groups (Fig. 3L and figs. S19 to S22). In addition, electron spin resonance (ESR) spectroscopy was used to evaluate the $^1O_2$ generation of TPAD-COF NPs under NIR laser illumination using 2,2,6,6-tetramethylpiperidine (TEMP) as a spin trap. After treatment with TPAD-COF NPs and 808-nm laser irradiation, a triplet ESR signal of the $^1O_2$/TEMP adduct with a relative intensity of 1:1:1 was monitored. In comparison, the ESR signals detected in the control and NIR laser exposure groups were negligible (Fig. 3M). To further confirm the effective $^1O_2$ production of TPAD-COF NPs during heating and cooling, the absorption intensity of DPBF gradually decreased with elevating temperature changes or increasing doses of TPAD-COF NP doses under NIR laser irradiation (figs. S23 to S25). These results confirmed that TPAD-COF NPs can rapidly convert temperature changes into pyroelectric charges under NIR laser irradiation, thereby enabling effective $^1O_2$ production. In addition to the production of $^1O_2$, we also identified the hydroxyl radical (•OH) and superoxide radical ($\bullet O_2^-$) generation, 5,5-dimethyl-1-pyrroline-*N*-oxide was used as a trapper to capture •OH and $\bullet O_2^-$, and similar results were also observed, with distinct •OH and $\bullet O_2^-$ ESR peaks detected in the presence of TPAD-COF NPs upon NIR laser exposure compared to the other groups. These findings validated the efficient generation of •OH and $\bullet O_2^-$ by TPAD-COF NPs under NIR laser illumination (fig. S26).

Furthermore, DFT calculations were conducted to propose the possible mechanism of ROS generation by TPAD-COF NPs under NIR laser irradiation (Fig. 3, N and O). The Gibbs free energy of the product is less than that of the reactants, and the energy drop further confirmed that the reaction favored the production of ROS, including $\bullet O_2^-$, $^1O_2$, and •OH (Fig. 3, P and Q). TPAD-COF NPs are excited to the excited singlet state (TPAD-COF NPs*) upon NIR laser irradiation, and TPAD-COF NPs may be evoked to produce electron-hole (e^-- h^+) pairs (Eq. 1, fig. S27). The resulting e^- may be captured by O_2 to generate $\bullet O_2^-$ with a reaction energy of −1.33 eV (Eq. 2; figs. S27 and S28), which was consistent with the redox potential. The CB bandgap of TPAD-COF was negatively larger than that of $O_2/\bullet O_2^-$. Thus,

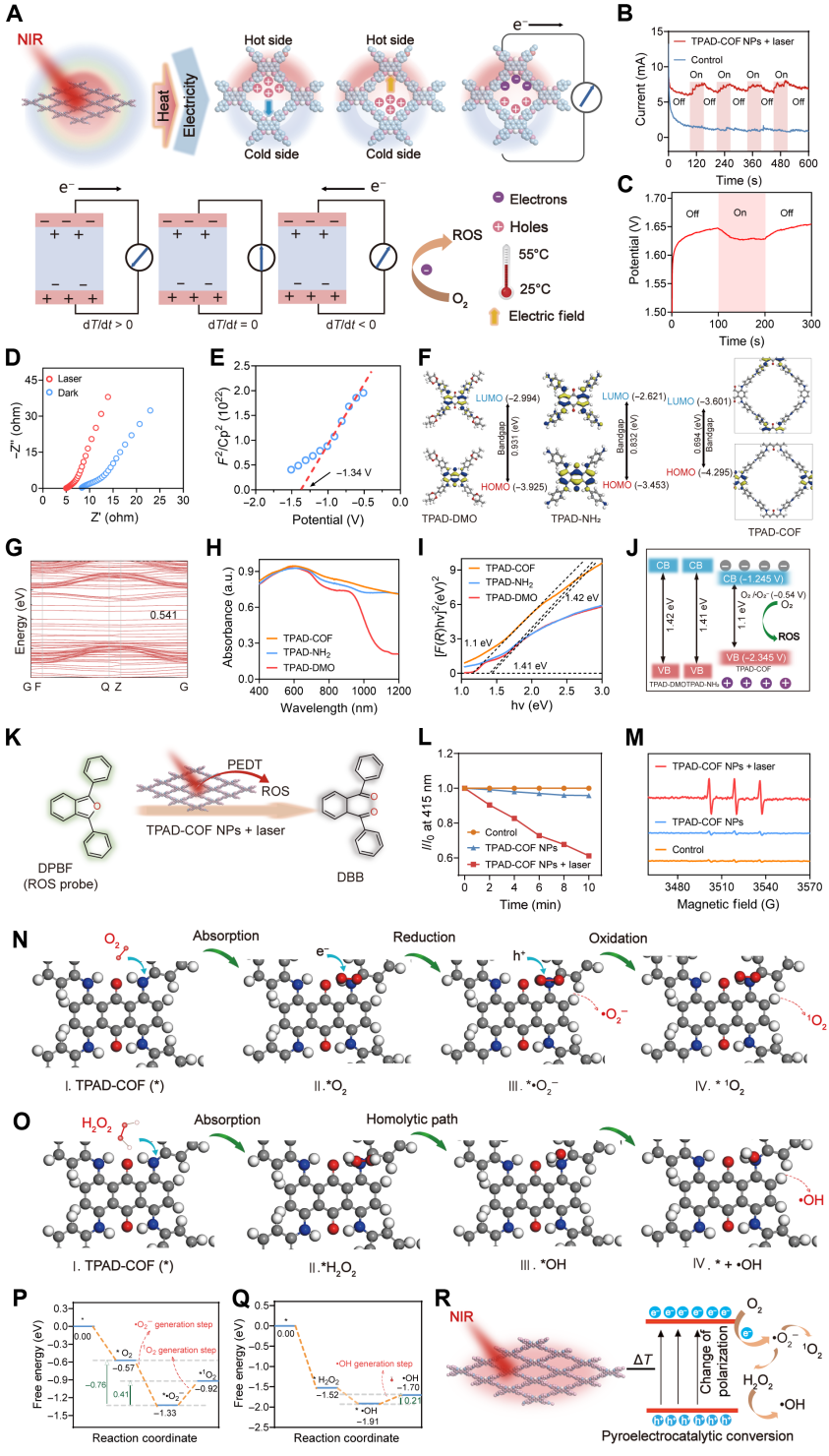

Fig. 3. PEDT effect and ROS generation of TPAD-COF NPs. (**A**) Scheme of the pyroelectric effect of TPAD-COF NPs under temperature variations and relationship between temperature variations (d*T*/d*t*) and pyroelectric currents. (**B**) Pyroelectric currents of TPAD-COF NPs under 5 laser on/off cycles. (**C**) Pyroelectric potentials and (**D**) EIS Nyquist plots of TPAD-COF NPs before and after 808-nm laser irradiation. (**E**) Mott-Schottky curve of TPAD-COF NPs. (**F**) The optimized molecular structures and calculated HOMO-LUMO energy gaps of TPAD-DMO, TPAD-NH_2, and TPAD-COF. (**G**) The electronic band structures of TPAD-COF. (**H**) UV-vis diffuse reflectance spectra of TPAD-DMO, TPAD-NH_2, and TPAD-COF. (**I**) Bandgaps of TPAD-DMO, TPAD-NH_2, and TPAD-COF. (**J**) Schematic illustration of the ROS generation mechanism. (**K**) Schematic representation of the $^1O_2$ detection mechanism of DPBF. (**L**) Normalized changes in the absorbance of DPBF solution at 415 nm after different treatments. (**M**) ESR spectra of different treatment groups. (**N** and **O**) Schematic illustration of the formation process of (N) $\cdot O_2^-$ and $^1O_2$, and (O) •OH. (**P** and **Q**) Reaction free energy plots of the (P) $\cdot O_2^-$ and $^1O_2$ and (Q) •OH generation process. (**R**) Scheme of ROS generation by TPAD-COF NPs under NIR laser exposure.

the pyroelectrically excited negative charge can react with O_2 in solution to form $\bullet O_2^-$. Moreover, $\bullet O_2^-$ is probably oxidized by trapped holes or valence band holes, to produce $^1O_2$ (Fig. 3, N and P, and fig. S27, Eq. 3). In addition, among the four major ROS, $\bullet O_2^-$ is second only to H_2O_2 in lifetime, and $\bullet O_2^-$ may become H_2O_2 through disproportionation (*47*). Furthermore, H_2O_2 can be further efficiently decomposed into •OH (Eqs. 4 to 6, fig. S27). The H_2O_2 molecule is absorbed at the active site (I) of TPAD-COF NPs with an absorption energy of −1.52 eV (II). The activated H_2O_2 is readily dissociated by homolysis, leading to the formation of 2 OH* (III). The hydroxyl group is then desorbed from the active site, producing active •OH and OH* (IV). The reaction energy of steps (I) to (IV) is −1.70 eV, which can be readily overcome at room temperature (Fig. 3, O and Q). Hence, TPAD-COF NPs can effectively facilitate the production of •OH by promoting H_2O_2 decomposition. Therefore, it can be speculated that the ROS production mechanism is accompanied by the adsorption of O_2, the reduction PEDT-induced electrons to $\bullet O_2^-$, and then the formation of $^1O_2$ and •OH by reduction-oxidation and disproportionation reactions (Fig. 3R) (*47*–*49*).

Cell uptake and antitumor effect of TPAD-COF NPs

Before in vitro therapeutic assessments, it is critical to validate whether TPAD-COF NPs can be internalized by 4T1 cells. Cyanine 5.5 (Cy5.5)–labeled TPAD-COF NPs were used to investigate their cell uptake at different incubation durations. Confocal laser scanning microscopy (CLSM) images indicated that the red fluorescence of Cy5.5-labeled TPAD-COF NPs increased with elevating incubation time, which were consistent with flow cytometry analysis (Fig. 4, A and C, and fig. S29). These findings illustrated that cellular internalization of TPAD-COF NPs exhibited an incubation duration–dependent pattern. Furthermore, the intracellular ROS generation of TPAD-COF NPs under NIR laser exposure was studied using 2′,7′-dichlorodihydrofluorescein diacetate (DCFH-DA) as a ROS probe. As displayed in Fig. 4B and fig. S30, a bright green fluorescent signal was detected in 4T1 cells after treatment with TPAD-COF NPs plus NIR laser irradiation. In contrast, no apparent green fluorescence was observed in the PBS-, laser-, and TPAD-COF NP-treated groups. In addition, the intracellular ROS level of the TPAD-COF NPs + laser group was 42.6%, which was distinctly higher than those of 3.37, 3.58, and 4.31% in the control, laser, and TPAD-COF NP groups, implying that TPAD-COF NPs can effectively convert temperature changes into intracellular ROS under NIR laser illumination (Fig. 4D and figs. S31 and S32).

Inspired by the effective cellular internalization of TPAD-COF NPs, the therapeutic effect of TPAD-COF NPs under NIR laser irradiation was investigated by the standard cell counting kit-8 (CCK-8) assay. The CCK-8 results showed that more than 80% of 4T1 cells survived after 24 hours of incubation with TPAD-COF NPs, even at 100 μg ml^{-1}, indicating that TPAD-COF NPs are highly cytocompatibility (Fig. 4E). Furthermore, irradiation by a NIR laser at diverse power densities did not markedly cause tumor cell death (Fig. 4F). Subsequently, the cytotoxic effects of TPAD-COF NPs under NIR laser irradiation were assessed, and their cell viability decreased substantially with elevating concentrations of TPAD-COF NPs upon NIR laser exposure (Fig. 4G). The survival of 4T1 cells was 30.1% after treatment with TPAD-COF NPs (100 μg ml^{-1}) plus 808-nm laser illumination. The median inhibitory concentration of TPAD-COF NPs was calculated to be 36.33 μg ml^{-1} under 808-nm laser exposure (fig. S33). Comparatively, negligible cytotoxic effect of TPAD-COF NPs on 4T1 cells was observed in the control, laser, and TPAD-COF NP groups (Fig. 4H). These results confirmed that TPAD-COF NP-mediated synergistic PEDT and PTT effects induced a substantial inhibitory effect on tumor cell proliferation. In addition, human umbilical cord endothelial cells were chosen to verify the cytocompatibility of TPAD-COF NPs in normal cells. As presented in fig. S34, no evident changes in the cell viability were observed after treatment with diverse doses of TPAD-COF NPs for 24 hours, indicating that TPAD-COF NPs were highly biocompatible with normal cells.

Furthermore, the in vitro therapeutic effect of TPAD-COF NPs under NIR laser illumination was assessed by live/dead staining. Live and dead cells are labeled with calcein–acetoxymethyl ester and propidium iodide, which appear as green and red fluorescence in CLSM images, respectively. Green fluorescence signals were visualized in the PBS-, laser-, and TPAD-COF NP-treated groups (Fig. 4I). In contrast, numerous dead cells with a distinct red fluorescence signal were recorded in the TPAD-COF NPs + laser group, indicating that TPAD-COF NPs effectively killed 4T1 cells by the synergistic PEDT and PTT effect under NIR laser exposure. Moreover, flow cytometry analysis was carried out to verify the activation of the apoptotic pathway by TPAD-COF NP incubation plus NIR laser illumination. Treatment with TPAD-COF NPs resulted in 59.8% of apoptotic cells after exposed to NIR laser irradiation, which was in accordance with CLSM results (Fig. 4, J and K). This demonstrated that TPAD-COF NPs triggered the synergistic PEDT and PTT effect upon NIR laser illumination, thus inducing impressive tumor cell apoptosis.

In vitro ICD effect induced by TPAD-COF NPs under NIR laser exposure

Therapeutic strategies, such as phototherapy and ROS-based therapies, have been validated to trigger ICD effect. Therefore, we explored the capacity of TPAD-COF NPs to elicit ICD occurrence under NIR laser illumination. The expression levels of ICD markers, such as calreticulin (CRT), high mobility group box 1 (HMGB1), and adenosine triphosphate (ATP), were measured. Immunofluorescence images revealed a notable increase in the fluorescence intensity of CRT protein after treatment with TPAD-COF NPs and NIR laser illumination, which were consistent with flow cytometry analysis results (Fig. 5, A and B, and figs. S35 and S36). In addition, only a weak HMGB1 fluorescence signal in nuclei was observed in the immunofluorescence images of the TPAD-COF NPs + laser group compared to the other groups (Fig. 5C). In addition, enzyme-linked immunosorbent assay (ELISA) was performed to detect HMGB1 levels in each treatment group, HMGB1 level was evidently highest in the TPAD-COF NPs + laser group, which was higher than those in the control, laser, and TPAD-COF NP groups (4.0-, 2.85-, and 1.9-fold, respectively) (Fig. 5D). Moreover, the intracellular ATP level in the TPAD-COF NPs + laser group declined markedly to 40.1% of the control group (Fig. 5E). In addition, in vitro immunofluorescence images of heat shock protein 90 (HSP90) expression revealed a prominent reduction in HSP90 expression in the TPAD-COF NPs + laser group, suggesting that the ROS generated by TPAD-COF NPs facilitated the decomposition of HSPs (fig. S37). These findings collectively confirmed that the synergistic PEDT and PTT effects mediated by TPAD-COF NPs overcame thermal resistance and triggered ICD effect under 808-nm laser exposure.

To assess the immunogenic effect mediated by TPAD-COF NPs under NIR laser exposure, bone marrow dendritic cells were isolated and then cocultured with 4T1 cells from each treatment group.

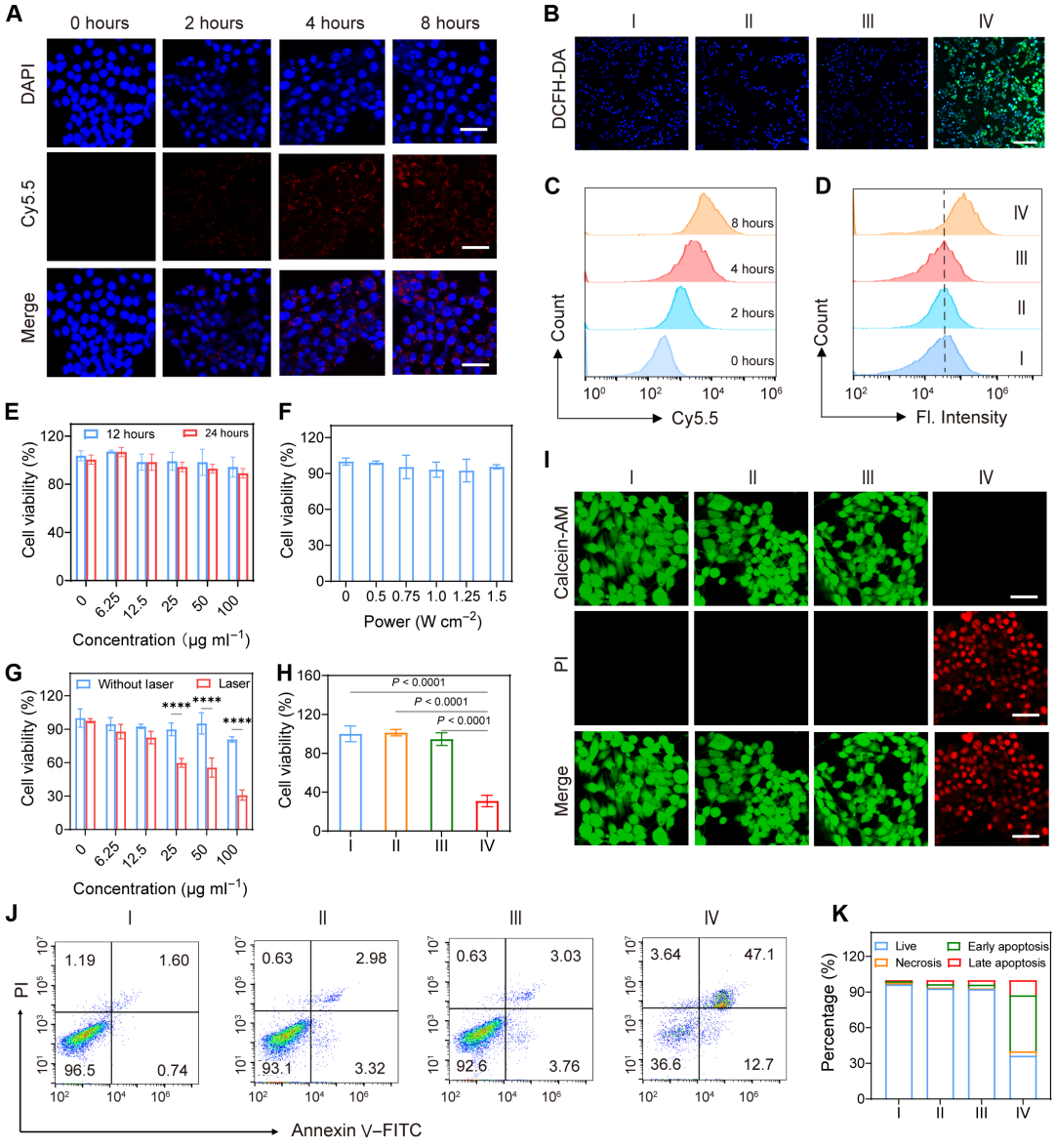

Fig. 4. Therapeutic effect of TPAD-COF NPs upon NIR irradiation in vitro. (**A**) Confocal images of 4T1 cells after 2, 4, and 8 hours of incubation with Cy5.5-labeled TPAD-COF NPs. Scale bars, 40 nm. (**B**) CLSM images of 4T1 cells stained with DCFH-DA in diverse treatment groups. Scale bar, 100 nm. (**C** and **D**) Flow cytometry analysis of (C) cellular uptake of TPAD-COF NPs ($n = 3$) and (D) ROS generation of TPAD-COF NPs in various treatment groups ($n = 3$). (**E** and **F**) Survival of 4T1 cells treatment with (E) elevated doses of TPAD-COF NPs for 12 and 24 hours and (F) a NIR laser at various power densities ($n = 5$). (**G** and **H**) Survival of 4T1 cells after treatment with (G) TPAD-COF NPs before and after NIR laser exposure ($n = 5$) and (H) varying disposes ($n = 5$). (**I**) Live/dead staining images in each group. Scale bars, 40 nm. (**J**) Flow cytometry analysis ($n = 3$) and (**K**) corresponding statistical analysis of cell apoptosis in each treatment group. I: Control; II: Laser (1.0 W cm^{-2}, 10 min); III: TPAD-COF NPs (100 μg ml^{-1}); IV: TPAD-COF NPs (100 μg ml^{-1}) + laser (1.0 W cm^{-2}, 10 min). Fl, fluorescence intensity; Calcein-AM, calcein–acetoxymethyl ester; PI, propidium iodide; FITC, fluorescein isothiocyanate.

The debris of 4T1 cells released abundant tumor-associated antigen, which then crossed the chamber membrane to promote dendritic cell (DC) maturation (Fig. 5, F and G). Thus, we performed flow cytometry analysis to evaluate DC maturation in each treatment group by labeling CD80 and CD86, respectively. Compared to other groups, TPAD-COF NPs effectively induced in vitro DC maturation with a proportion of 27.6%, which was obviously higher than those of 8.1, 9.6, and 13.5% in the control, laser, and TPAD-COF NP groups (Fig. 5, H and I). This suggested that ICD effect mediated by TPAD-COF NPs facilitated DC maturation under NIR laser exposure. Subsequently, the secreted levels of immunostimulatory cytokines, including interleukin-6 (IL-6), IL-12, interferon-γ (IFN-γ), and TNF-α, were measured by ELISA (Fig. 5, J to M). The levels of these cytokines in the TPAD-COF NPs + laser group were distinctly higher than those in other treatment groups, indicating that TPAD-COF NP-mediated synergistic PEDT and PTT effects induced DC maturation for immunostimulatory cytokine secretion.

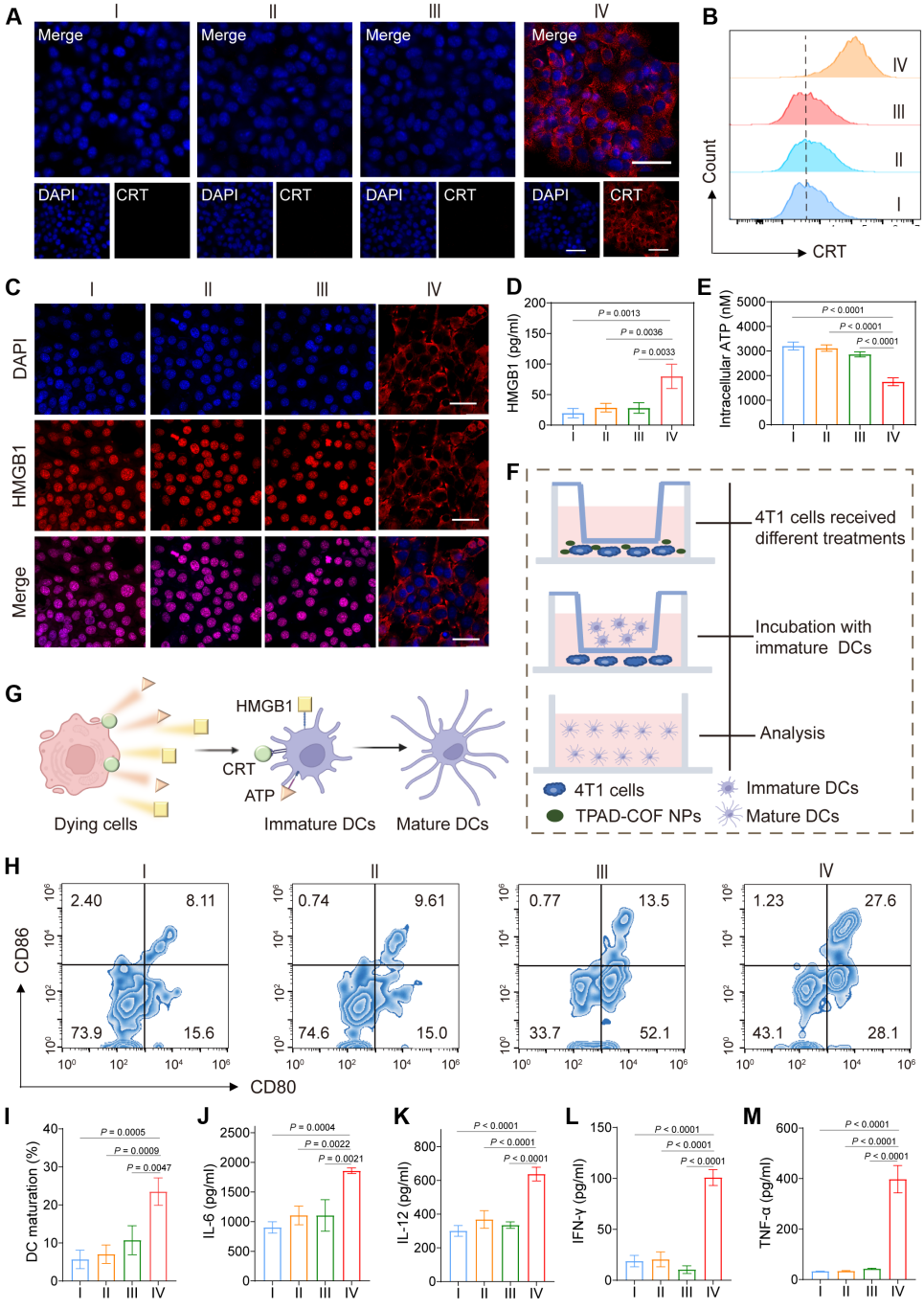

Fig. 5. TPAD-COF NP-mediated immune response upon NIR laser irradiation in vitro. (**A**) Immunofluorescence images and (**B**) flow cytometry analysis of CRT in 4T1 cells after various treatments. (**C**) Immunofluorescence images and (**D**) ELISA analysis of HMGB1 in 4T1 cell supernatant after diverse treatments ($n = 3$). (**E**) Intracellular ATP content of 4T1 cells in different treatment groups ($n = 3$). (**F**) Scheme of the coincubation system of immature DCs and 4T1 cells. (**G**) The schedule mechanism of DC maturation triggered by DAMPs. (**H**) Flow cytometry analysis and (**I**) statistical analysis of DC maturation in different treatment groups ($n = 3$). (**J** to **M**) The secreted levels of cytokines ($n = 3$), including (J) IL-6, (K) IL-12, (L) IFN-γ, and (M) TNF-α, in different treatment groups. I: Control; II: Laser; III: TPAD-COF NPs (100 μg ml^{-1}); IV: TPAD-COF NPs (100 μg ml^{-1}) + laser (1.0 W cm^{-2}, 10 min).

In vivo antitumor effect of TPAD-COF–mediated PEDT under NIR laser irradiation

The satisfactory in vitro therapeutic effect encouraged us to investigate the in vivo antitumor performance of TPAD-COF NPs under NIR laser irradiation. Before this, the hemolytic activity of TPAD-COF NPs was assessed to verify their hemocompatibility. Even at 500 μg ml^{-1}, the hemolysis of TPAD-COF NPs was negligible, suggesting that TPAD-COF NPs are highly hemocompatible (fig. S38). The biodistribution and systemic toxicity of TPAD-COF NPs in vivo were studied to evaluate their biocompatibility and further translational applications. Mice bearing 4T1 tumors were intravenously injected with Cy5.5-labled TPAD-COF NPs and

then monitored by in vivo fluorescence imaging. TPAD-COF NPs passively accumulated into tumor tissues and reached their highest at 6 hours (Fig. 6A and fig. S39). In addition, at 24 hours postinjection, ex vivo fluorescence images of tumors and major organs further verified the effective tumor enrichment of TPAD-COF NPs (fig. S40). Subsequently, the toxicity of TPAD-COF NPs was investigated by hematoxylin and eosin (H&E) staining of main organs from various groups. As shown in fig. S41, H&E staining images revealed negligible obvious tissue inflammation in each treatment group. In addition, routine blood analysis and biochemical tests also showed no abnormal variations in representative parameters after treatment with TPAD-COF NPs (figs. S42 and S43). These results verified the high biocompatibility of TPAD-COF NPs for subsequent therapeutic evaluation. To prove the ROS-facilitated decomposition of HSPs in tumor tissues, the expression of HSP90 in each group was verified by immunofluorescence assay. The results demonstrated that HSP90 expression was obviously decreased in the TPAD-COF NPs + laser group in comparison to the other three groups (fig. S44).

The treatment efficacy of TPAD-COF NP-mediated synergistic effects of PEDT and PTT was investigated in vivo. 4T1 tumor mice with a size of approximately 100 mm^3 were randomized into four groups ($n = 5$), including control, laser, TPAD-COF NP, and TPAD-COF NPs + laser groups (Fig. 6B). As shown in Fig. 6C, the body weight fluctuations of mice were negligible after various treatments, indicating high biocompatibility of TPAD-COF NPs. In addition, the temperature changes of the tumor site in each treatment group were monitored by a thermal camera. The tumor temperatures in the TPAD-COF NPs + laser group elevated rapidly and reached 57.7°C within 10 min, while the tumor temperature in the control group changed slightly under the same irradiation condition, suggesting that TPAD-COF NPs manifested favorable capacity to facilitate photothermal conversion and thereby lead to prominent PEDT effect in vivo (Fig. 6, D and E). Furthermore, the changes in tumor volumes of the mice from each group were plotted to evaluate the treatment outcome of synergistic effects of PEDT and PTT. The most obvious treatment efficacy was observed in the TPAD-COF NPs + laser group, with a tumor inhibition rate of 99.7% after 16 days of observation, while no conspicuous suppression was visualized in the other groups (Fig. 6, F to H). In addition, the representative photographs and average weights of the resected tumors intuitively revealed that TPAD-COF NPs and NIR laser irradiation–mediated therapeutic outcome was much higher than those in the other groups, benefiting from the synergistic thermal effect and abundant ROS generation mediated by TPAD-COF NPs under NIR laser exposure (Fig. 6, I and J).

To clarify the potential therapeutic mechanism of TPAD-COF NPs under NIR laser exposure, dihydroethidium staining was performed to measure the ROS production in tumor tissues. Apparently, a negligible red fluorescence can be observed in the control, laser, and TPAD-COF NP groups, while bright red fluorescence was visualized in the TPAD-COF NPs + laser group (Fig. 6K). Furthermore, H&E, terminal deoxynucleotidyl transferase–mediated deoxyuridine triphosphate nick end labeling, and Ki-67 staining was carried out to assess the therapeutic effect after diverse treatments. More apoptotic cells and fewer Ki-67–positive cells were observed in the staining images of tumor tissues in the TPAD-COF NPs + laser group compared to other three groups, confirming that TPAD-COF NP-mediated synergistic PEDT and PTT effects inhibited tumor cell proliferation (Fig. 6L). In addition, negligible pathological signals were visualized in the H&E staining images of the main organs in various groups, verifying the high biocompatibility of TPAD-COF NPs for potential antitumor application (fig. S45).

Effectiveness of TPAD-COF NPs on distal tumor inhibition under NIR laser illumination

The high frequency of tumor recurrence poses a tremendous challenge to conventional tumor treatment strategies. After realizing the impressive treatment effect on primary tumor suppression, we subsequently expanded the evaluation of the efficacy of TPAD-COF NP-mediated PEDT and PTT effects on distal tumor inhibition using a bilateral tumor mouse model (Fig. 7A). When the sizes of primary tumors reached around 100 mm^3, the mice were injected intravenously with TPAD-COF NPs. NIR irradiation was applied to the primary tumors rather than distant tumors. The bilateral tumor size and body weight in different treatment groups were monitored. The growth curves of bilateral tumors in Fig. 7 (B and C) indicated that TPAD-COF NPs markedly suppressed primary and distant tumor proliferation upon NIR irradiation, with tumor growth inhibition (TGI) rates of 92.5 and 58.5%, respectively (Fig. 7, D and E, and figs. S46 and S47). Subsequently, the bilateral tumors collected in each treatment group were weighed and photographed, and the smallest primary and distant tumors were observed in the TPAD-COF NPs + laser group, with the lightest average weights of 0.06 and 0.34 g, respectively (Fig. 7, F to I). In addition, negligible body weight variation was detected in all treatment groups, indicating the high biosafety of TPAD-COF NP injection and NIR laser exposure (Fig. 7J). Furthermore, the immune activation induced by TPAD-COF NPs and NIR laser exposure was verified by immunohistochemical and immunofluorescence staining of tumor tissues from diverse treatment groups. As displayed in Fig. 7K, obviously elevated CRT exposure and markedly reduced HMGB1 expression could be observed from the immunofluorescence images in the TPAD-COF NPs + laser group. In addition, compared to the control, laser, and TPAD-COF NP groups, immunofluorescence images clearly exhibited increased $CD4^+$ and $CD8^+$ T cell infiltration in tumors after treatment with TPAD-COF NPs and NIR laser exposure (Fig. 7L). These findings suggested that TPAD-COF NPs in combination with NIR laser illumination exhibited the best therapeutic effect on distant tumors, which was attributed to the highly efficient immune activation of the TPAD-COF NPs + laser group.

To further investigate the antitumor immunogenicity of TPAD-COF NPs upon NIR laser exposure, the proportions of DCs, CD4 T cells, CD8 T cells, regulatory T cells (T_{regs}), and myeloid-derived suppressor cells (MDSCs) were studied by flow cytometry. As presented in Fig. 7M, an evident elevation in mature DCs was measured in the lymph nodes of the mice from TPAD-COF NPs + laser group, accounting for 29.7%, indicating that TPAD-COF NP-mediated synergistic PEDT and PTT effects effectively induced DC maturation. In addition, the levels of CD4 helper T lymphocyte and CD8 cytotoxic T lymphocyte (20.4 and 10.0% in spleen; 36.3 and 16.6% in tumor tissues) in the TPAD-COF NPs + laser group were apparently higher than in those in other treatment groups, suggesting that TPAD-COF NPs manifested high capability in eradicating tumors by triggering the occurrence of ICD upon NIR laser irradiation (Fig. 7, N and O, and figs. S48 and S49). Moreover, treatment with TPAD-COF NPs and subsequent NIR laser illumination led to a marked reduction in the proportion of MDSCs (11.4%) compared to that (32.8%) in the PBS-treated group (Fig. 7P). In addition, the percentages of T_{regs} in tumors tissues from TPAD-COF NPs + laser group were evidently

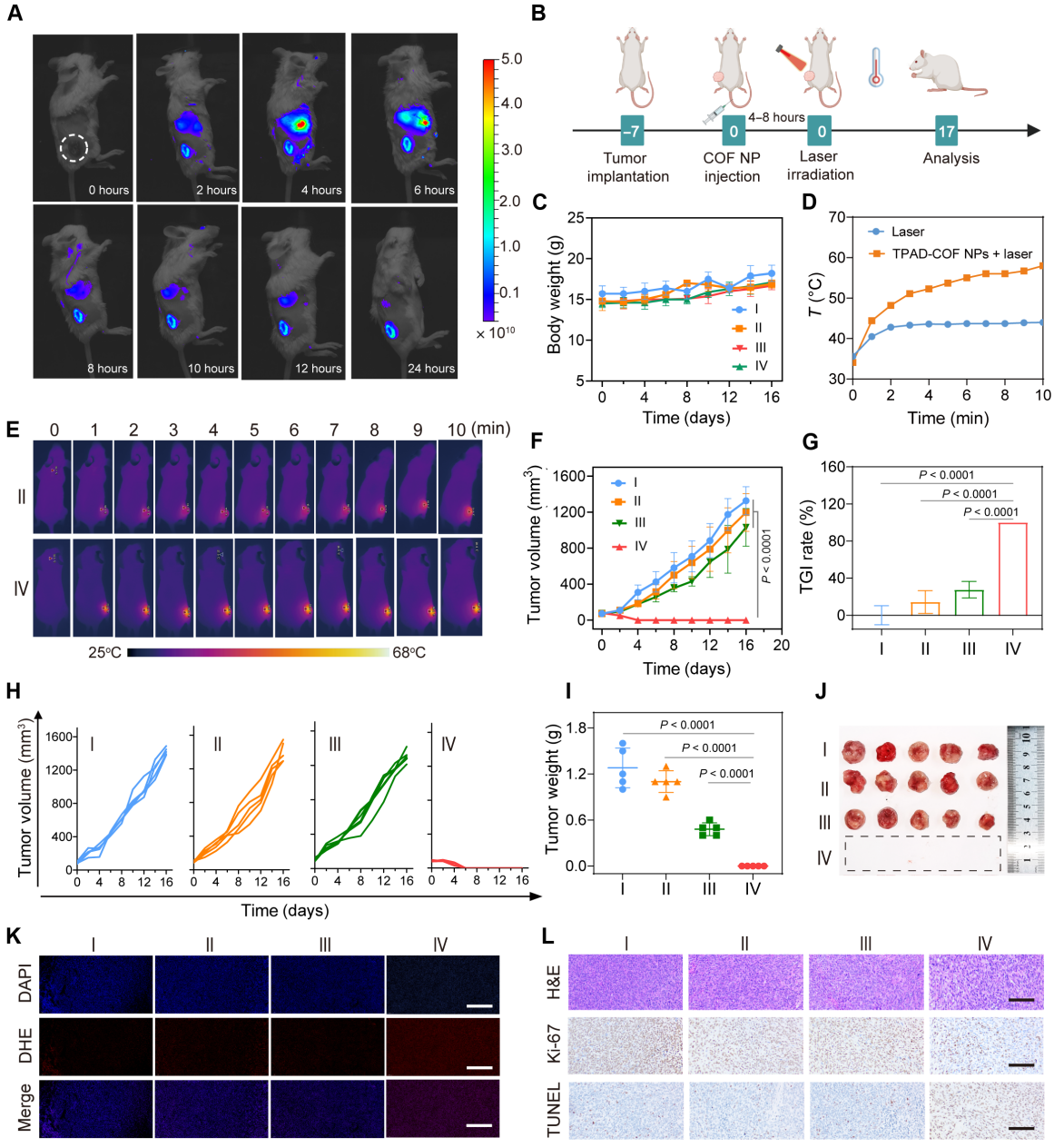

Fig. 6. In vivo antitumor effect of TPAD-COF NPs upon NIR exposure. (**A**) Fluorescence images of mice after tail vein injection of Cy5.5-labeled TPAD-COF NPs for varying durations. (**B**) Scheme of the treatment process in vivo. (**C**) Body weights of mice in diverse groups ($n = 5$). (**D**) Tumor temperature curves of mice and (**E**) corresponding thermal images in the laser and TPAD-COF NPs + laser groups. (**F**) Tumor volumes, (**G**) TGI rates, and (**H**) individual tumor volumes ($n = 5$). (**I**) Tumor weights and (**J**) digital photograph of tumors after diverse treatments ($n = 5$). (**K**) Immunofluorescence images of ROS and (**L**) H&E, terminal deoxynucleotidyl transferase–mediated deoxyuridine triphosphate nick end labeling (TUNEL), and Ki-67 antibody staining images of tumor slices after diverse treatments. Scale bars, 100 μm. I: Control; II: Laser (1.0 W cm^{-2}, 10 min); III: TPAD-COF NPs (100 μg ml^{-1}); IV: TPAD-COF NPs (100 μg ml^{-1}) + laser (1.0 W cm^{-2}, 10 min).

decreased to 12.2% compared to 19.2% of the control group (Fig. 7Q). These results confirmed that TPAD-COF NP-mediated synergistic PEDT and PTT effects elicited an antitumor immune response.

Antitumor effect of TPAD-COF NPs on the prevention of lung metastasis under NIR irradiation

Distant metastasis remains one of the primary causes of clinical treatment failure (*50*). Inspired by the effective activation of systemic immune response induced by TPAD-COF NPs under NIR laser exposure, the ability of TPAD-COF NPs to prevent lung metastasis under NIR laser irradiation was studied using a lung metastasis model (Fig. 8A). After various treatments, the weight fluctuations of mice were ignored, indicating that TPAD-COF nanoparticles had high biocompatibility (Fig. 8B). Lung metastasis was prominently suppressed in the TPAD-COF NPs + laser group, with a substantial reduction of 80% in the number of metastatic nodules after treatment with

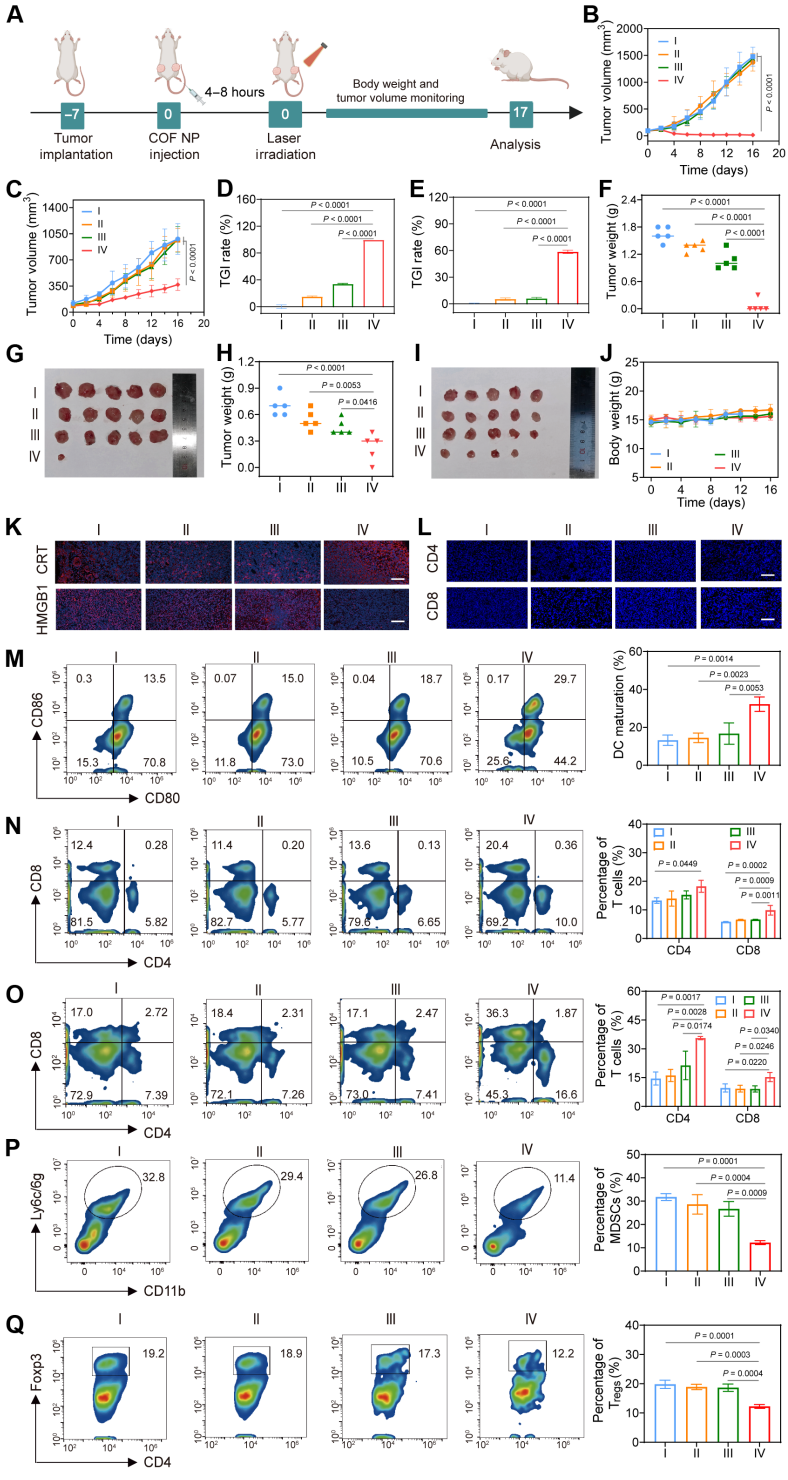

Fig. 7. TPAD-COF NP-mediated therapeutic effect on a bilateral tumor-bearing mouse model under NIR laser exposure. (**A**) Scheme of bilateral tumor model establishment and subsequent treatment process. (**B** and **C**) Volume curves of the (B) primary and (**C**) distant tumors after diverse treatments ($n = 5$). (**D** and **E**) TGI rate of (D) primary and (E) distant tumors in diverse treatment groups ($n = 5$). (**F**) Tumor weight and (**G**) digital photograph of primary tumors after various treatments ($n = 5$). (**H**) Tumor weight and (**I**) digital photograph of distant tumors in each treatment group ($n = 5$). (**J**) Body weight of mice in different groups ($n = 5$). (**K** and **L**) Immunofluorescence images of (K) CRT and HMGB1 and (L) $CD4^+$ and $CD8^+$ T cells in tumor tissues after various treatments. Scale bars, 100 μm. (**M**) DC maturation in lymph nodes after diverse treatments and corresponding statistical analysis by flow cytometry ($n = 3$). (**N** and **O**) $CD4^+$ and $CD8^+$ T cells in the (N) spleen and (O) tumor tissues after different treatments and corresponding statistical analysis ($n = 3$). (**P**) MDSCs in tumor tissues and (**Q**) T_{regs} in tumor tissues from each treatment group and the corresponding statistical analysis ($n = 3$). I: Control; II: Laser (1.0 W cm^{-2}, 10 min); III: TPAD-COF NPs; IV: TPAD-COF NPs (100 μg ml^{-1}) + laser (1.0 W cm^{-2}, 10 min).

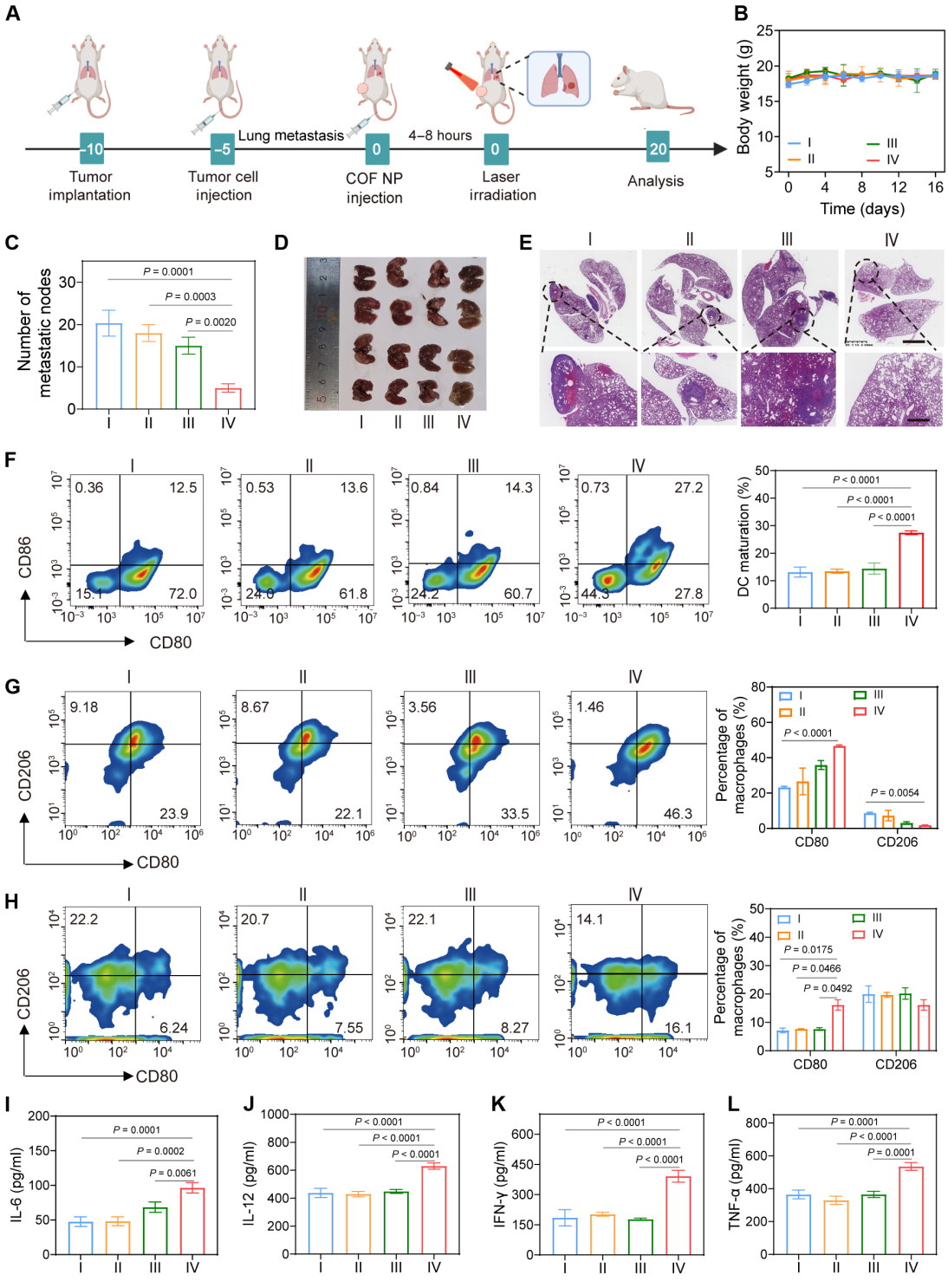

Fig. 8. Therapeutic effect of TPAD-COF NPs on a pulmonary metastasis model under NIR laser irradiation. (**A**) Scheme of lung metastasis model establishment and treatment process. (**B**) Mouse body weights ($n = 5$), (**C**) number of metastatic nodes in lung tissues ($n = 4$), (**D**) digital photograph of the dissected lung tissues ($n = 4$), and (**E**) H&E staining images of the lung tissues after different treatments. (**F**) Flow cytometry analysis and corresponding statistical analysis of DC maturation in tumor tissues of each group ($n = 3$). (**G** and **H**) Flow cytometry analysis of M1 and M2 macrophage proportions in (G) tumor tissues and (H) spleen tissues after different treatments and the corresponding statistical analysis ($n = 3$). (**I** to **L**) The secreted levels of cytokines ($n = 3$), including (I) IL-6, (J) IL-12, (K) INF-γ, and (L) TNF-α after diverse treatments [I: Control; II: Laser (1.0 W cm^{-2}, 10 min); III: TPAD-COF NPs (100 μg ml^{-1}); IV: TPAD-COF NPs (100 μg ml^{-1}) + laser (1.0 W cm^{-2}, 10 min)].

TPAD-COF NPs and NIR laser exposure (Fig. 8C). In addition, digital photographs and H&E staining images of the excised lung tissues suggested that treatment with TPAD-COF NPs and NIR laser illumination led to an apparent decline in metastatic tumor lesions compared to those in other treatment groups (Fig. 8, D and E). These findings suggested that TPAD-COF NP-mediated and NIR laser–triggered synergistic PEDT and PTT effects effectively triggered immune response, thus prominently delaying the progression of lung metastasis.

Subsequently, the maturation of DCs in tumor tissues in each treatment group was investigated. Flow cytometry analysis exhibited that the percentage of DCs in the TPAD-COF NPs + laser group was 27.2%, which was evidently higher than that in the control (12.5%), TPAD-COF NP (13.6%), and laser (14.3%) groups, suggesting that TPAD-COF NP-mediated synergistic PEDT and PTT effects facilitated ICD activation in vivo, thus promoting DC maturation (Fig. 8F). Furthermore, we evaluated the effects of TPAD-COF NPs on remodeling the immune microenvironment under NIR laser irradiation. A distinct increase in the proportion (46.3 and 16.1%, respectively) of tumor-suppressing M1 macrophages can be observed in tumors and spleen tissues in the TPAD-COF NPs + laser group (Fig. 8, G and H). In addition, ELISA was used to measure the expression levels of cytokines related to antitumor activity. Notably, a marked enhancement in the expression of IL-6, IL-12, TNF-α, and IFN-γ was detected in the TPAD-COF NPs + laser group in comparison with that in the PBS-treated group (Fig. 8, I to L). These results demonstrated that TPAD-COF NPs can effectively reprogram the suppressive immune microenvironment upon NIR laser exposure, thereby augmenting antitumor immunity.

Mechanistic analysis of TPAD-COF NPs on tumor metastasis

Transcriptome sequencing analysis was carried out on 4T1 cells in the TPAD-COF NPs + laser and control groups to disclose the potential antitumor mechanism of TPAD-COF NPs under NIR laser exposure. Venn analysis identified the differentially expressed genes (DEGs) between the TPAD-COF NPs + laser and control groups (Fig. 9A). Compared to the control group, approximately 342 genes were dysregulated in the TPAD-COF NPs + laser group, including 265 up-regulated and 77 down-regulated genes, among which DEGs were identified via the screening criteria [fold change ≥ 2.0 (or -2.0), $P < 0.05$] (Fig. 9, B and C). In addition, the genes associated with oxidative stress, apoptosis, and immune response were enumerated in the heatmap (Fig. 9D). Among these dysregulated genes, the down-regulation of *NQO1* could promote the conversion of quinone into semihydroquinone through single electron reduction reaction, which then can produce ROS through the redox cycle (*51*). The apoptosis-related genes such as *CXCL10* and *TNFSF10* were obviously up-regulated in the TPAD-COF NPs + laser group, suggesting that TPAD-COF NPs + laser–mediated synergistic PEDT and PTT effects caused obvious tumor cell apoptosis (*52*). In addition, up-regulation of *CXCL10* can also promote T cell expression and migration to tumors, thereby activating immune response and improving antitumor efficacy (*53*).

Kyoto Encyclopedia of Genes and Genomes (KEGG) pathway and gene ontology (GO) analyses were performed on these DEGs to better comprehend how TPAD-COF NPs acted on 4T1 cells via synergistic PEDT and PTT effects upon NIR laser exposure. As presented in Fig. 9E, GO annotation analysis illustrated that treatment with TPAD-COF NPs and NIR laser exposure distinctly changed the expression of genes participated diverse biological processes, including immune processes, biological regulation, metabolic processes, and cellular processes. In addition, KEGG analysis revealed that pathways related to apoptosis, metastasis, and immune response were apparently enriched in the TPAD-COF NPs + laser group, including FOXO signaling pathway, TNF signaling pathway, JAK-STAT signaling pathway, and MHC-I and MHC-II pathways (Fig. 9F). These pathways are correlated with cellular physiological events, including apoptosis, cell cycle control, antioxidative stress, and immune responses. For instance, FOXO signaling pathway can promote apoptosis via activating the expression of many apoptosis-related genes, such as *TNFSF10* (*54*). Up-regulation of MHC-I molecules such as H2-T24 can promote the recognition of tumor cells by cytotoxic $CD8^+$T cells (*55*). In addition, radical s-adenosyl methionine domain containing 2 (*RSAD2*), which is necessary to achieve DC maturation through interferon regulatory factor 7–mediated signaling pathway, was also up-regulated in the TPAD-COF NPs + laser group (*56*). In addition, Toll-like receptor (TLR) pathways and retinoic acid-inducible gene-I (RIG-I)–like receptor pathways changed in the TPAD-COF NPs + laser group, TLRs are members of the pattern recognition receptor family that can bind to endogenous damage associated molecular patterns (DAMPs) such as HMGB1 and then activate the immune response (*57*). Next, the chord diagram was analyzed, which further showed the interaction between different proteins and pathways (Fig. 9G). Therefore, the above results revealed that TPAD-COF NPs can cause apoptosis, inhibit tumor cell growth, and activate the immune system under NIR laser irradiation, thus leading to notable tumor suppression.

DISCUSSION

In summary, we have successfully developed a distinct nCOF-based pyroelectric catalyst for pyroelectric catalysis-activated in situ immunotherapy. By confining organic pyroelectric molecules in the rigid nCOFs, TPAD-COF NPs reduced molecular aggregation and improved aqueous solubility, thus maximizing the exposure of the catalytic active sites to the substrate (O_2) and enhancing the efficiency of pyroelectric catalysis. After internalization by tumors, TPAD-COF NPs effectively generated thermal effect and thus led to ICD activation. In addition, TPAD- COF NPs facilitated the catalytic conversion of temperature changes into pyroelectric charges, which then interacted with adjacent O_2 for rapid ROS generation, thereby augmenting ICD activation. In vivo investigation using distant tumor and lung metastasis models confirmed that treatment with TPAD-COF NPs and NIR laser irradiation prominently inhibited growth of primary and distant tumors as well as obviously delayed lung metastasis. RNA profiling revealed that TPAD-COF NP administration evidently caused the enrichment of apoptosis, metastasis, and immune-response pathways. Thus, this research provided a distinct avenue to develop nCOF-based pyroelectric catalyst to effectively combat tumor metastasis with high safety and efficiency.

MATERIALS AND METHODS

Synthesis of TPAD-DMO

1,4,5,8-Tetrachloro-9,10-anthracenedione (391 mg, 1.13 mmol), 4-(5,5-dimethyl-1,3-dioxan-2-yl) aniline (1.4 g, 6.75 mmol), and Cs_2CO_3 (2.95 g, 9.04 mmol) were added in anhydrous toluene (50 ml) under argon atmosphere. After argon bubbling for 20 min, $Pd_2(dba)_3$ (42 mg, 4 mol %) and 2,2′-bis(diphenylphosphino)-1,1′-binaphthalene (BINAP; 124 mg, 12 mol %) were added to the above solution. The

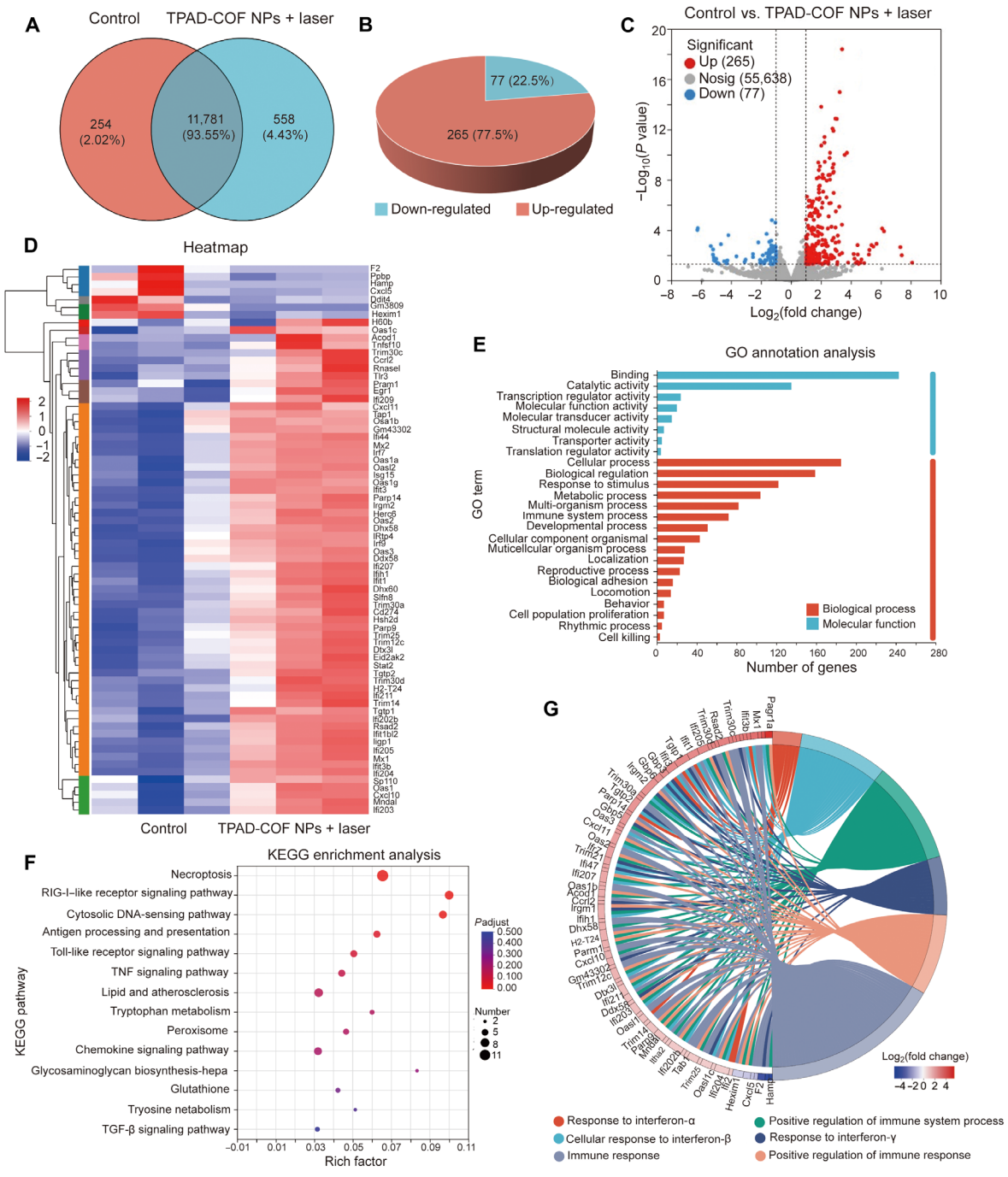

Fig. 9. Transcriptome sequencing analysis of the mechanism of TPAD-COF NPs under 808-nm laser irradiation. (**A**) Venn analysis, (**B**) pie chart, and (**C**) volcano plot of DEGs in the control and TPAD-COF NPs + laser groups. (**D**) Heatmap of the DEGs related to the immune response. (**E**) GO annotation analysis of the DEGs and the 25 most significantly enriched categories. (**F**) KEGG pathway enrichment analysis of the DEGs. (**G**) Protein-protein interaction network involved in the immune response and TNF signaling pathways. TGF-β, transforming growth factor–β.

mixture was kept at 110°C for 48 hours under stirring (fig. S1). The solvent was removed after cooling. Dichloromethane/petroleum ether (2:3) was used as the eluent, and the obtained solid was purified by neutral alumina chromatography to obtain a dark green solid as the product (2.41 g, 78%). ^{1}H nuclear magnetic resonance (NMR) [400 MHz, dimethyl sulfoxide (DMSO)–d_6] δ 11.68 (s, 4H), 7.75 (s, 4H), 7.41 (d, J = 28.0 Hz, 8H), 7.20 (d, J = 11.8 Hz, 8H), 5.36 (s, 4H), 3.66 (d, J = 10.4 Hz, 8H), 3.60 (d, J = 13.8 Hz, 8H), 1.17 (d, J = 13.2 Hz, 12H), 0.76 (s, 12H). ^{13}C NMR (150 MHz, DMSO-d_6) δ 190.0, 149.4, 131.8, 127.9, 127.5, 122.0, 121.0, 113.5, 102.0, 77.1, 30.3, 23.2, and 21.9. High-resolution mass spectrometry (HRMS) (ESI): mass/charge ratio (m/z) $[M + H]^+$ calcd. for $C_{62}H_{69}N_4O_{10}^+$: 1029.4856; found: 1029.5005.

Synthesis of TPAD-NH_2

Synthesis of TPAD-NHBoc

1,4,5,8-tetrachloro-9,10-anthracenedione (1 g, 2.89 mmol), tert-butyl *N*-(4-aminophenyl) carbamate (3.6 g, 17.34 mmol), and Cs_2CO_3 (7.54 g, 23.12 mmol) were added in anhydrous toluene (50 ml) under argon atmosphere. After argon bubbling for 20 min, $Pd_2(dba)_3$ (110 mg, 4 mol %) and BINAP (330 mg, 12% mol) were added to the above solution, and the mixture was stirred at 110°C for 48 hours (fig. S2). The solvent was removed after cooling. The resulting solid was purified by neutral alumina column chromatography, and dichloromethane was used as the eluent to obtain a dark green solid (1.78 g, 59%). ^{1}H NMR (400 MHz, DMSO-d_6) δ 11.76 (s, 4H), 9.37 (s, 4H), 7.48-7.42 (m, 12H), 7.19 (d, J = 6.0 Hz, 8H), 1.48 (s, 36H).

Synthesis of TPAD-NH_2

At 0°C, trifluoroacetic acid (2.8 ml, 36 mmol) was dispersed to a dichloromethane (100 ml) solution of TPAD-NHBoc (1 g, 0.97 mmol) under argon atmosphere, and the solution was stirred overnight at 25°C. The resulting suspension was filtered and washed with an aqueous solution of saturated sodium bicarbonate (fig. S2). The solid was then acidified and neutralized with 1.2 M hydrochloric acid and 5 M sodium hydroxide aqueous solutions, respectively. The solution was filtered and rinsed with deionized water, cold methanol, and dichloromethane to obtain a black solid as the product (400 mg in 65% yield). ^{1}H NMR (400 MHz, DMSO-d_6) δ 11.69 (s, 4H), 7.23-6.59 (m, 20H), 5.07 (s, 8H). ^{13}C NMR (150 MHz, DMSO-d_6) δ 184.2, 146.5, 143.3, 128.5, 126.0, 123.2, 115.9, 115.1, and 112.4. HRMS (ESI): m/z [M + H] $^+$ calcd. for $C_{38}H_{33}N_8O_2^+$: 633.2569; found: 633.2725.

Synthesis of TPAD-COF

TPAD-DMO (51.4 mg, 0.05 mmol) and TPAD-NH_2 (31.6 mg, 0.05 mmol) were added to the Pyrex tube, followed by mesitylene (1 ml) and dioxane (1 ml). After 1 min of sonication, 0.3 ml of 6.0 M acetic acid aqueous solution was added. The solution was resonicated for 1 min and further degassed through three freeze-pump-thaw cycles, purged with argon, and then heated at 120°C for 3 days (fig. S3). The green precipitate was harvested by sucking filtration and sequentially washed with *N*,*N*-dimethylformamide, absolute ethanol, and acetone. The precipitate was then dried under vacuum for 24 hours to obtain a green powder with a yield of 50%. ^{13}C cross polarization-magic angle spinning NMR (125 MHz, solid state): δ (parts per million) 149.5, 143.0, 133.8, 131.9, 127.3, 123.8, and 118.4.

Synthesis of TPAD-COF NPs

To disperse the TPAD-COF sample in PBS solution, 10 mg of TPAD-COF and 20 mg of DSPE-PEG-NH_2 (molecular weight = 2000) were dispersed in PBS (20 ml) and then sonicated over 24 hours by a 900-W ultrasonic cell grinder (fig. S4). The resulting solution was first centrifuged at 1500 rpm for 30 min to discard the unmodified nanoparticles, followed by centrifugation at 11,000 rpm for 10 min to obtain TPAD-COF NPs.

In vitro photothermal performance evaluation

The gradient concentrations of TPAD-COF NP solutions were exposed to an 808-nm laser (1.5 W cm^{-2}) irradiation for 10 min, and the temperature variations of the TPAD-COF NP solutions were monitored by a thermal camera. In addition, TPAD-COF NP solutions (300 μg ml^{-1}) were irradiated with an 808-nm laser with diverse power densities for 10 min, and the corresponding solution temperature was recorded.

The photothermal conversion efficiency (η) of TPAD-COF NPs was determined by recording the temperature change of TPAD-COF NPs (300 μg ml^{-1}) solution as a function of irradiation duration during heating and cooling. The η of TPAD-COF NPs was determined by the previously reported method (*58*). As shown in Fig. 2N, τ_s was determined to be 220. In addition, the m_i and $C_{p,i}$ were 0.2 g and 4.2 J/g. Therefore, hS = 3.8 mW/°C. ΔT_{max} was calculated to be 33.4°C. Therefore, the η was determined to be 29.1%.

In vitro ROS generation

DPBF (40 μg ml^{-1}, 3 ml) aqueous solutions containing TPAD-COF NPs were exposed to alternating NIR laser irradiation (1.0 W cm^{-2}) or various temperatures for various durations, and the absorption spectra of different durations were recorded. ESR spectroscopy measurements were performed using TEMP as a $^1O_2$ trap. The solution in each treatment group (PBS, TPAD-COF NPs, and TPAD-COF NPs + laser) was mixed with TEMP solution (20 μl, 1 M) in a vail, respectively. Subsequently, the ESR signal of each group was monitored using an ESR spectrometer.

Cellular uptake of TPAD-COF NPs

4T1 cells were inoculated into confocal dishes (10^5 cells per dish) overnight and then cultured with Cy5.5-labeled TPAD-COF NPs for diverse incubation times (0, 2, 6, and 8 hours), respectively. After rinsed with PBS, the cells were labeled with 4′,6-diamidino-2-phenylindole (DAPI) and subsequently visualized by CLSM.

For semiquantitative analysis of cellular uptake, 4T1 cells were seeded into six-well plates overnight, followed by 0, 2, 4, and 8 hours of incubation with Cy5.5-labeled TPAD-COF NPs, respectively. Afterward, the cells were rinsed, trypsinized, and quantified by flow cytometry.

Cytotoxicity assessment

To assess the cytotoxicity of TPAD-COF NPs, 4T1 cells (10^4 cells per well) were cultured overnight in 96-well plates and incubated with various doses of TPAD-COF NPs. Then, the cell survival of TPAD-COF NPs was detected using the CCK-8 assay.

To evaluate the antitumor effect of TPAD-COF NPs under NIR laser exposure, 4T1 cells were cultured with diverse doses of TPAD-COF NPs for 6 hours and then exposed to a NIR laser. In addition, the cells received various treatments, including PBS, laser, TPAD-COF NPs, and TPAD-COF NPs + laser, and the cell viabilities after various treatments were determined.

In vitro ICD biomarker detection

4T1 cells were cultured in six-well plates overnight. After different treatments (PBS, laser, TPAD-COF NPs, and TPAD-COF NPs + laser), the cells were fixed and immersed in immunostaining blocking solution for 20 min at 4°C. After removing the blocking solution, the cells were cultured with CRT and HMGB1 rabbit monoclonal antibody (1:200) overnight at 4°C. Afterward, the cells were cultured with 1 ml of Alexa Fluor 488–conjugated goat anti-rabbit immunoglobulin G (1:300) for 1 hour. After rinsed with PBS, the cells were labeled with DAPI for 30 min and then observed by CLSM. In addition, the ATP assay was conducted in accordance with the manufacturer's instructions.

In vitro DC maturation evaluation

4T1 cells were administrated with different treatments and then cocultured with immature DCs for 48 hours. Subsequently, the nonadherent cells from each group were harvested, labeled with anti–CD80-phycoerythrin, anti–CD86-allophycocyanin, and anti–CD11–fluorescein isothiocyanate, and rinsed with PBS for flow cytometry analysis. In addition, the proinflammatory cytokines in DC suspensions were measured by ELISA kits.

In vivo antitumor efficacy

All the animal studies were approved by the Committee on the Ethics of Animal Experiments of Shanghai University (approval no. ECSHU 2021–050). Mice bearing tumors were randomized into four groups ($n = 5$), including control (100 μl of PBS), laser (1.0 W cm^{-2}, 10 min), TPAD-COF NPs (20 mg kg^{-1}), and TPAD-COF NPs (20 mg kg^{-1}) + laser (1.0 W cm^{-2}, 10 min) groups. Tumor volumes and mouse body weights were recorded. After 16 days of different treatments, the tumors of each group were harvested for histological analysis. In addition, the main organs in various groups were collected for H&E staining.

Effectiveness of TPAD-COF NPs on distant tumor inhibition under NIR laser irradiation

To evaluate the therapeutic effect of TPAD-COF NPs on distant tumor suppression under NIR laser irradiation, 5×10^5 and 1×10^6 cells were injected to the left and right flanks of Balb/c mice, respectively, to establish a bilateral tumor model. When the size of primary tumors was approximately 100 mm^3, the mice were randomized into four groups ($n = 5$) and treated as follows, including control, laser (1.0 W cm^{-2}, 10 min), TPAD-COF NPs (20 mg kg^{-1}), and TPAD-COF NPs (20 mg kg^{-1}) + laser (1.0 W cm^{-2}, 10 min). After 4 hours of injection, the primary tumors in the laser and TPAD-COF NPs + laser groups were irradiated by an 808-nm laser for 10 min. After various treatments, the size of primary and distant tumors and mouse body weight of mice were monitored every 2 days. On the 17th day, the mice were euthanized, and the lymph nodes, tumors, spleen, serum, and major organs of each group were collected for analysis, respectively.

Effectiveness of TPAD-COF NPs in preventing lung metastasis under NIR laser irradiation

A 4T1 tumor–bearing mouse model was constructed through subcutaneous injection of 4T1 cells (10^6 cells per mouse) into the right hind leg. When the size of tumors reached nearly 50 mm^3, mice were administrated intravenously with 10^5 cells to construct a lung metastasis model. Mice were randomly divided into four groups ($n = 5$) to receive diverse treatments, including control, laser (1.0 W cm^{-2}, 10 min), TPAD-COF NPs (20 mg kg^{-1}), and TPAD-COF NPs (20 mg kg^{-1}) + laser (1.0 W cm^{-2}, 10 min) groups. Last, the mice were euthanized, and the lungs and tumors of each group were collected to assess the therapeutic effect of TPAD-COF NPs in delaying lung metastasis under NIR laser irradiation.

Statistical analysis

All data were presented as mean ± SD and analyzed using GraphPad Prism 7.4.0. The significance of the data was evaluated according to the unpaired Student's two-sided test, two-way analysis of variance (ANOVA) test, or one-way ANOVA test. $^{****}P < 0.0001$.

Supplementary Materials

This PDF file includes:

Supplementary Text
Figs. S1 to S49

REFERENCES AND NOTES

1. Y. Dong, S. Dong, C. Yu, J. Liu, S. Gai, Y. Xie, Z. Zhao, X. Qin, L. Feng, P. Yang, Y. Zhao, Mitochondria-targeting Cu_3VS_4 nanostructure with high copper ionic mobility for photothermoelectric therapy. *Sci. Adv.* **9**, eadi9980 (2023).
2. X. Ji, Z. Tang, H. Liu, Y. Kang, L. Chen, J. Dong, W. Chen, N. Kong, W. Tao, T. Xie, Nanoheterojunction-mediated thermoelectric strategy for cancer surgical adjuvant treatment and β-elemene combination therapy. *Adv. Mater.* **35**, 2207391 (2022).
3. Y. Wang, X. Dai, C. Dong, W. Guo, Z. Xu, Y. Chen, H. Xiang, R. Zhang, Engineering electronic band structure of binary thermoelectric nanocatalysts for augmented pyrocatalytic tumor nanotherapy. *Adv. Mater.* **34**, e2106773 (2022).
4. X. Yuan, Y. Kang, J. Dong, R. Li, J. Ye, Y. Fan, J. Han, J. Yu, G. Ni, X. Ji, D. Ming, Self-triggered thermoelectric nanoheterojunction for cancer catalytic and immunotherapy. *Nat. Commun.* **14**, 5140 (2023).
5. W. Huang, L. He, Z. Zhang, S. Shi, T. Chen, Shape-controllable Tellurium-driven heterostructures with activated robust immunomodulatory potential for highly efficient radiophotothermal therapy of colon cancer. *ACS Nano* **15**, 20225–20241 (2021).
6. X. Wu, M. Wen, Y. Zou, X. Gao, C. Wei, R. Liu, J. Li, L. Wang, X. Li, Y.-N. Liu, W. Chen, Cold-catalytic antitumor immunity with pyroelectric black phosphorus nanosheets. *Chem. Sci.* **13**, 6842–6851 (2022).
7. S. Zhu, R. Tian, A. L. Antaris, X. Chen, H. Dai, Near-infrared-II molecular dyes for cancer imaging and surgery. *Adv. Mater.* **31**, e1900321 (2019).
8. W. Li, S. Yin, Y. Shen, H. Li, L. Yuan, X.-B. Zhang, Molecular engineering of pH-responsive NIR oxazine assemblies for evoking tumor ferroptosis via triggering lysosomal dysfunction. *J. Am. Chem. Soc.* **145**, 3736–3747 (2023).
9. C. S. Diercks, O. M. Yaghi, The atom, the molecule, and the covalent organic framework. *Science* **355**, eaal1585 (2017).
10. K. Geng, T. He, R. Liu, S. Dalapati, K. Tan, Z. Li, S. Tao, Y. Gong, Q. Jiang, D. Jiang, Covalent organic frameworks: Design, synthesis, and functions. *Chem. Rev.* **120**, 8814–8933 (2020).
11. A. P. Côté, A. I. Benin, N. W. Ockwig, M. O'Keeffe, A. J. Matzger, O. M. Yaghi, Porous, crystalline, covalent organic frameworks. *Science* **310**, 1166–1170 (2005).
12. C. Wang, Z. Lv, W. Yang, X. Feng, B. Wang, A rational design of functional porous frameworks for electrocatalytic CO_2 reduction reaction. *Chem. Soc. Rev.* **52**, 1382–1427 (2023).
13. W. Zhang, L. Chen, S. Dai, C. Zhao, C. Ma, L. Wei, M. Zhu, S. Y. Chong, H. Yang, L. Liu, Y. Bai, M. Yu, Y. Xu, X.-W. Zhu, Q. Zhu, S. An, R. S. Sprick, M. A. Little, X. Wu, S. Jiang, Y. Wu, Y.-B. Zhang, H. Tian, W.-H. Zhu, A. I. Cooper, Reconstructed covalent organic frameworks. *Nature* **604**, 72–79 (2022).
14. D. Chen, W. Chen, Y. Wu, L. Wang, X. Wu, H. Xu, L. Chen, Covalent organic frameworks containing dual O_2 reduction centers for overall photosynthetic hydrogen peroxide production. *Angew. Chem. Int. Ed.* **62**, e202217479 (2023).
15. J. N. Chang, J. W. Shi, Q. Li, S. Li, Y. R. Wang, Y. Chen, F. Yu, S. L.-L. Li, Y.-Q. Lan, Regulation of redox molecular junctions in covalent organic frameworks for H_2O_2 photosynthesis coupled with biomass valorization. *Angew. Chem. Int. Ed.* **62**, e202303606 (2023).
16. Z.-B. Zhou, P.-J. Tian, J. Yao, Y. Lu, Q.-Y. Qi, X. Zhao, Toward azo-linked covalent organic frameworks by developing linkage chemistry via linker exchange. *Nat. Commun.* **13**, 2180 (2022).
17. Q. Zhang, S. Dong, P. Shao, Y. Zhu, Z. Mu, D. Sheng, T. Zhang, X. Jiang, R. Shao, Z. Ren, J. Xie, X. Feng, B. Wang, Covalent organic framework–based porous ionomersfor high-performance fuel cells. *Science* **378**, 181–186 (2022).
18. S. S. A. Shah, M. S. Javed, T. Najam, M. A. Nazir, A. u. Rehman, A. Rauf, M. Sohail, F. Verpoort, S.-J. Bao, Covalent organic frameworks (COFs) for heterogeneous catalysis: Recent trends in design and synthesis with structure-activity relationship. *Mater. Today* **67**, 229–255 (2023).
19. S. An, Q. Xu, Z. Ni, J. Hu, C. Peng, L. Zhai, Y. Guo, H. Liu, Construction of covalent organic frameworks with crown ether struts. *Angew. Chem. Int. Ed.* **60**, 9959–9963 (2021).
20. M. Sun, Z. Liu, L. Wu, J. Yang, J. Ren, X. Qu, Bioorthogonal-activated in situ vaccine mediated by a COF-based catalytic platform for potent cancer immunotherapy. *J. Am. Chem. Soc.* **145**, 5330–5341 (2023).
21. L.-L. Zhou, Q. Guan, Y. B. Dong, Covalent organic frameworks: Opportunities for rational materials design in cancer therapy. *Angew. Chem. Int. Ed.* **63**, e202314763 (2023).
22. L. Zhang, S. Wang, Y. Zhou, C. Wang, X.-Z. Zhang, H. Deng, Covalent organic frameworks as favorable constructs for photodynamic therapy. *Angew. Chem. Int. Ed.* **58**, 14213–14218 (2019).
23. L. Zhang, S.-C. Wan, J. Zhang, M.-J. Zhang, Q.-C. Yang, B. Zhang, W.-Y. Wang, J. Sun, R. T. K. Kwok, J. W. Y. Lam, H. Deng, Z.-J. Sun, B. Tang, Activation of pyroptosis using AIEgen-based sp^2 carbon-linked covalent organic frameworks. *J. Am. Chem. Soc.* **145**, 17689–17699 (2023).

24. L. Chen, W. Wang, J. Tian, F. Bu, T. Zhao, M. Liu, R. Lin, F. Zhang, M. Lee, D. Zhao, X. Li, Imparting multi-functionality to covalent organic framework nanoparticles by the dual-ligand assistant encapsulation strategy. *Nat. Commun.* **12**, 455 (2021).
25. Y. He, Z. Li, C. Cong, F. Ye, J. Yang, X. Zhang, Y. Yuan, Z. Ma, K. Zhang, Y. Lin, L. Zheng, X.-J. Liang, D. Gao, Pyroelectric catalysis-based "nano-lymphatic" reduces tumor interstitial pressure for enhanced penetration and hydrodynamic therapy. *ACS Nano* **15**, 10488–10501 (2021).
26. Y. Chang, Y. Cheng, R. Zheng, X. Wu, P. Song, Y. Wang, J. Yan, H. Zhang, Plasmon-pyroelectric nanostructures used to produce a temperature-mediated reactive oxygen species for hypoxic tumor therapy. *Nano Today* **38**, 101110 (2021).
27. X. Li, M.-L. Gao, S.-S. Wang, Y.-L. Li, T.-N. Liu, H. Xiang, P.-N. Liu, Engineering an organic nanoplatform for augmented pyroeletroimmunotherapy. *Adv. Mater.* **36**, 2400756 (2024).
28. P. S. Steeg, Targeting metastasis. *Nat. Rev. Cancer* **16**, 201–218 (2016).
29. G. Bergers, S.-M. Fendt, The metabolism of cancer cells during metastasis. *Nat. Rev. Cancer* **21**, 162–180 (2021).
30. P. Zhang, Y. Zhai, Y. Cai, Y. Zhao, Y. Li, Nanomedicine-based immunotherapy for the treatment of cancer metastasis. *Adv. Mater.* **31**, e1904156 (2019).
31. J. Nam, S. Son, L. J. Ochyl, R. Kuai, A. Schwendeman, J. J. Moon, Chemo-photothermal therapy combination elicits anti-tumor immunity against advanced metastatic cancer. *Nat. Commun.* **9**, 1074 (2018).
32. A. Ribas, J. D. Wolchok, Cancer immunotherapy using checkpoint blockade. *Science* **359**, 1350–1355 (2018).
33. R. Eil, S. K. Vodnala, D. Clever, C. A. Klebanoff, M. Sukumar, J.-H. Pan, D. C. Palmer, A. Gros, T. N. Yamamoto, S. J. Patel, G. C. Guittard, Z. Yu, V. Carbonaro, K. Okkenhaug, D. S. Schrump, W. M. Linehan, R. Roychoudhuri, N. P. Restifo, Ionic immune suppression within the tumour microenvironment limits T cell effector function. *Nature* **537**, 539–543 (2016).
34. M. He, K. Roussak, F. Ma, N. Borcherding, V. Garin, M. White, C. Schutt, T. I. Jensen, Y. Zhao, C. A. Iberg, K. Shah, H. Bhatia, D. Korenfeld, S. Dinkel, J. Gray, A. U. Antonova, S. Ferris, D. Donermeyer, C. L. Arlehamn, M. M. Gubin, J. Luo, L. Gorvel, M. Pellegrini, A. Sette, T. Tung, R. Bak, R. L. Modlin, R. C. Fields, R. D. Schreiber, P. M. Allen, E. Klechevsky, CD5 expression by dendritic cells directs T cell immunity and sustains immunotherapy responses. *Science* **379**, eabg2752 (2023).
35. R. M. Steinman, J. Banchereau, Taking dendritic cells into medicine. *Nature* **449**, 419–426 (2007).
36. D. V. Krysko, A. D. Garg, A. Kaczmarek, O. Krysko, P. Agostinis, P. Vandenabeele, Immunogenic cell death and DAMPs in cancer therapy. *Nat. Rev. Cancer* **12**, 860–875 (2012).
37. R. Li, F. Yang, L. Zhang, M. Li, G. Wang, W. Wang, Y. Xu, W. Wei, Manipulating host-guest charge transfer of a water-soluble double-cavity cyclophane for NIR-II photothermal therapy. *Angew. Chem. Int. Ed.* **62**, e202301267 (2023).
38. Y. Ding, Z. Sun, Y. Gao, S. Zhang, C. Yang, Z. Qian, L. Jin, J. Zhang, C. Zeng, Z. Mao, W. Wang, Plasmon-driven catalytic chemotherapy augments cancer immunotherapy through induction of immunogenic cell death and blockage of IDO pathway. *Adv. Mater.* **33**, e2102188 (2021).
39. B. Ding, P. Zheng, F. Jiang, Y. Zhao, M. Wang, M. Chang, P'a. Ma, J. Lin, MnO_x nanospikes as nanoadjuvants and immunogenic cell death drugs with enhanced antitumor immunity and antimetastatic effect. *Angew. Chem. Int. Ed.* **59**, 16381–16384 (2020).
40. C. Zhang, Z. Zeng, D. Cui, S. He, Y. Jiang, J. Li, J. Huang, K. Pu, Semiconducting polymer nano-PROTACs for activatable photo-immunometabolic cancer therapy. *Nat. Commun.* **12**, 2934 (2021).
41. J. Fucikova, O. Kepp, L. Kasikova, G. Petroni, T. Yamazaki, P. Liu, L. Zhao, R. Spisek, G. Kroemer, L. Galluzzi, Detection of immunogenic cell death and its relevance for cancer therapy. *Cell Death Dis.* **11**, 1013 (2020).
42. C. Ji, W. Cheng, Q. Yuan, K. Müllen, M. Yin, From dyestuff chemistry to cancer theranostics: The rise of rylenecarboximides. *Acc. Chem. Res.* **52**, 2266–2277 (2019).
43. L. Yang, B. Huang, S. Hu, Y. An, J. Sheng, Y. Li, Y. Wang, N. Gu, Indocyanine green assembled free oxygen-nanobubbles towards enhanced near-infrared induced photodynamic therapy. *Nano Res.* **15**, 4285–4293 (2022).
44. J. Zeng, D. Goldfeld, Y. Xia, A plasmon-assisted optofluidic (PAOF) system for measuring the photothermal conversion efficiencies of gold nanostructures and controlling an electrical switch. *Angew. Chem. Int. Ed.* **52**, 4169–4173 (2013).
45. C. M. Hessel, V. P. Pattani, M. Rasch, M. G. Panthani, B. Koo, J. W. Tunnell, B. A. Korgel, Copper selenide nanocrystals for photothermal therapy. *Nano Letters* **11**, 2560–2566 (2011).
46. M. Wang, B. Wang, F. Huang, Z. Lin, Enabling PIEZOpotential in PIEZOelectric semiconductors for enhanced catalytic activities. *Angew. Chem. Int. Ed.* **58**, 7526–7536 (2019).
47. Y. Nosaka, A. Y. Nosaka, Generation and detection of reactive oxygen species in photocatalysis. *Chem. Rev.* **117**, 11302–11336 (2017).
48. C. Lu, C. Zhang, P. Wang, Y. Zhao, Y. Yang, Y. Wang, H. Yuan, S. Qu, X. Zhang, G. Song, K. Pu, Light-free generation of singlet oxygen through manganese-thiophene nanosystems for pH-responsive chemiluminescence imaging and tumor therapy. *Chem* **6**, 2314–2334 (2020).
49. X. Wang, K. Ma, T. Goh, M. R. Mian, H. Xie, H. Mao, J. Duan, K. O. Kirlikovali, A. E. B. S. Stone, D. Ray, M. R. Wasielewski, L. Gagliardi, O. K. Farha, Photocatalytic biocidal coatings featuring Zr_6Ti_4-based metal–organic frameworks. *J. Am. Chem. Soc.* **144**, 12192–12201 (2022).
50. Y. Fernández, J. Cueva, A. G. Palomo, M. Ramos, A. de Juan, L. Calvo, J. García-Mata, P. García-Teijido, I. Peláez, L. García-Estévez, Novel therapeutic approaches to the treatment of metastatic breast cancer. *Cancer Treat. Rev.* **36**, 33–42 (2010).
51. K.-A. Jung, M.-K. Kwak, The Nrf2 system as a potential target for the development of indirect antioxidants. *Molecules* **15**, 7266–7291 (2010).
52. M. Pan, X. Wei, X. Xiang, Y. Liu, Q. Zhou, W. Yang, Targeting CXCL9/10/11–CXCR3 axis: An important component of tumor-promoting and antitumor immunity. *Clin. Transl. Oncol.* **25**, 2306–2320 (2023).
53. B. L. Rodriguez, D. L. Gibbons, MEK inhibition invigorates chemoimmunotherapy by tumor mitophagy-induced CXCL10 expression. *Cell Rep. Med.* **3**, 100506 (2022).
54. M. Farhan, H. Wang, U. Gaur, P. J. Little, J. Xu, W. Zheng, FOXO signaling pathways as therapeutic targets in cancer. *Int. J. Biol. Sci.* **13**, 815–827 (2017).
55. K. L. Rock, E. Reits, J. Neefjes, Present yourself! by MHC class I and MHC class II molecules. *Trends Immunol.* **37**, 724–737 (2016).
56. J.-S. Jang, J.-H. Lee, N.-C. Jung, S.-Y. Choi, S.-Y. Park, J.-Y. Yoo, J.-Y. Song, H.-G. Seo, H.-S. Lee, D.-S. Lim, *Rsad2* is necessary for mouse dendritic cell maturation via the IRF7-mediated signaling pathway. *Cell Death Dis.* **9**, 823 (2018).
57. W. Ren, L. Zhao, Y. Sun, X. Wang, X. Shi, HMGB1 and Toll-like receptors: Potential therapeutic targets in autoimmune diseases. *Mol. Med.* **29**, 117 (2023).
58. J. Li, J. Wang, J. Zhang, T. Han, X. Hu, M. M. S. Lee, D. Wang, B. Z. Tang, A facile strategy of boosting photothermal conversion efficiency through state transformation for cancer therapy. *Adv. Mater.* **33**, e2105999 (2021).

Acknowledgments: We thank the Research Center of Analysis and Test of East China University of Science and Technology for help in the characterization. **Funding:** This work was supported by National Natural Science Foundation of China (nos. 22201073, 21925201, 22161160319, T2322018, and 32171391), Shanghai Rising-Star Program (22QA1403600), and the Fundamental Research Funds for the Central Universities. **Author contributions:** Conceptualization: H. X., P.-N.L., and X.L. Methodology: X.L., M.-L.G., P.-N.L., and H.X. Investigation: X.L., M.-L.G., S.-S.W., Y.H., and D.H. Visualization: X.L., M.-L.G., S.-S.W., P.-N.L., and H.X. Writing (original draft): X.L., M.-L.G., P.-N.L., and H.X. Writing (review and editing): X.L., M.-L.G., S.-S.W., P.-N.L., and H.X. Supervision: H.X., P.-N.L., and X.L. **Competing interests:** The authors declare that they have no competing interests. **Data and materials availability:** All data needed to evaluate the conclusions in the paper are present in the paper and/or the Supplementary Materials.

Submitted 4 July 2024
Accepted 25 October 2024
Published 29 November 2024
10.1126/sciadv.adr5145